Stony Brook University

The official electronic file of this thesis or dissertation is maintained by the University Libraries on behalf of The Graduate School at Stony Brook University.

A deconvolution method for switching current histograms as a fast diagnosis tool

A Thesis Presented

by

Dirk Bluhm

to

The Graduate School

in Partial Fulfillment of the Requirements

for the Degree of

Master of Arts

in

Physics

Stony Brook University

August 2008

Stony Brook University

The Graduate School

Dirk Bluhm

We, the thesis committee for the above candidate for the Master of Arts degree, hereby recommend acceptance of this thesis.

Dr. James E. Lukens – Thesis Advisor
Professor, Department of Physics and Astronomy

Dr. Harold J. Metcalf – Chairperson of Defense
Distinguished Teaching Professor, Department of Physics and Astronomy

Dr. Matthew Dawber
Assistant Professor, Department of Physics and Astronomy

This thesis is accepted by the Graduate School.

Lawrence Martin
Dean of the Graduate School

Abstract of the Thesis

A deconvolution method for switching current histograms as a fast diagnosis tool

by

Dirk Bluhm

Master of Arts

in

Physics

Stony Brook University

2008

Modern physics likes to probe quantum behavior on a macroscopic scale. An example for such a device is the rf-SQUID, also considered as a qubit for quantum computing. The rf-SQUID consists of a superconducting loop, interrupted by an insulating barrier. This barrier is known as Josephson junction and allows for some tunneling current. By biasing the rf-SQUID with half a flux quantum, the potential energy of the qubit forms a double well potential that can be treated like the harmonic oscillator with small corrections. For temperatures between 1.3 K and 530 mK, we measured thermal escape rates from one potential well to the other in dependence of the qubit bias flux, using this as an indicator for sample quality. Together with the fast diagnosis setup that allowed for careful measurements and a new method of deconvoluting switching current histograms, a fast turn-around process for sample quality characterization has been established.

Contents

List of Figures

Acknowledgements

Writing acknowledgements was the part I enjoyed most about writing my thesis, mostly because it gave me a wonderful opportunity to say "thank you" to people who mean something to me, who helped me in various situations or have just spent a good amount of time with me.

In the academic environment, among a number of teachers, I want to stress Harold Metcalf's role. He taught me that science is not only a formula, but also a story to be told. In our lab, I mostly worked with Doug Bennett and Luigi Longobardi, who helped me with my thesis project. I owe Luigi many thanks for carefully reviewing this thesis. The work was supported in many ways by Shawn Pottorf, Esteban Monge, Vijay Patel, Pete Davis and Pernille Jensen, and it would have not been possible without Jim Lukens' advices.

I am grateful to Fakher Assaad, Laszlo Mihaly and Pat Peiliker who organized the exchange program between Würzburg University and Stony Brook.

Each of the friends I made at Stony Brook would deserve his own paragraph. I am very grateful for all the hours I spent at "The Manchester", and I was not expecting its inhabitants making it to be so hard to leave for me. Thanks to Sara, Poppy, Burton, Marlin, Robert and Paul.

Simon and Uvo who came with me the long way over the Atlantic Ocean were fixed points in all the rough times in the beginning, as was my friend Olga.

Three very close friends from High School are to mention at this point who have accompanied my life since then with humor, quips and great support. It seems that we will stay widespread over the planet for a while, but thanks to modern communication technology I don't have to abstain from Ansgar, David and Stefan.

Last to acknowledge is the support I got from my family all over the years. My parents Marion and Klaus have always been on my side, and backed every one of my decisions. It feels very good having such a loving sister as Alina.

Jonas showed me that love can withstand a long distance, and I am glad to come back to live with him.

This work has been partially supported by the DAAD (German Academic Exchange Service) and my adviser Jim Lukens.

Chapter 1

Introduction and Background

1.1 Introduction

After Heike Kamerlingh Onnes was the first to liquefy Helium in 1908, he opened the wide field of low temperature physics that gives basic insights for our understanding of matter. Using his ability to achieve low temperatures, he discovered (1911) the abrupt disappearance of resistance in a sample of mercury and stated [4]:

> "Mercury has passed into a new state, which on account of its extraordinary electrical properties may be called the superconductive state."

After lossless conductivity had been found, Meissner and Ochsenfeld [5] found that superconductors are also perfect diamagnets (1933). Magnetic fields do hardly penetrate superconductors, and a field in an originally normal sample is expelled when the temperature falls down through T_c, the so called critical temperature, where a normal conductor turns superconducting. The London equations [6] yield that a magnetic field is exponentially screened from the interior of a superconductor with penetration depth λ. This implies that both high temperature and high magnetic fields can destroy superconductivity. Empiric studies show that the critical field is approximated by a parabolic law:

$$H_c(T) \approx H_c(0)[1 - (T/T_c)^2] \tag{1.1}$$

After the first description of its basic electrodynamic properties by London and London 1935, superconductivity was later explained by Ginzburg and Landau 1950 (GL-theory, macrocopic effects) and Bardeen, Cooper and Schrieffer 1957 (BCS-theory) [7], who proposed Cooper pairs were responsible for superconductivity. The founders of the latter theory were awarded a Nobel Prize in

1

1972, as was Ginzburg in 2003. Landau was awarded a Nobel Prize in 1962, for "for his pioneering theories for condensed matter, especially liquid helium" [8]. This section intends to give a short overview on superconductivity, following the very comprehensive book of Tinkham [9], and then provides some closer view on the superconducting quantum interference devices (SQUIDs) based on Josephson junctions used in this research, namely the rf- and the dc-SQUID.

1.2 Bardeen-Cooper-Schrieffer and Ginzburg-Landau theories

The development of the BCS theory was driven by two major observations that had to be explained: First, the Meissner-Ochsenfeld-effect, and second, the observation that the critical temperature of the metal is depending on its isotopic mass ($T_c \cdot \sqrt{M} = const.$). Furthermore, it had to explain the second order phase transition at the critical temperature occuring in the electron gas. There was also evidence for an energy gap for single-particle like excitation, e.g. the electronic specific heat varying as $exp(T_0/T)$ near T=0 K.

The relation between critical temperature and mass suggests that phonons are involved in the mechanism that leads to superconductivity. The first electron causes (since it has negative charge) a small deformation in the crystal lattice as it moves along. This deformation acts like a funnel for a second electron with opposite spin, it moves than in the region with higher positive charge density. This process is only possible if the energies of the system are small, e.g. thermal oscillations do not need to be taken into account and the current density is low enough.

The two electrons form so called "Cooper pairs" with total spin $s = 0$. As a pair they no longer act as fermions but rather they obey Bose-statistics. Thus, the Pauli principle no longer applies and they can be in the same quantum state. Not only that is energetically more favorable, it also results in a Bose-Einstein-wavefunction through the whole superconductor. The formation of the Cooper pairs causes an energy gap to appear around the Fermi energy, bigger than the energy transmitted to an electron by colliding with a lattice atom. Therefore, there are no scattering states and local interactions with impurities can not influence this wavefunction, thus currents do not experience resistance.

Based on the theory of phase transitions and thermodynamics, Ginzburg and Landau derived some macroscopic properties of superconductors. As a result of their theory they introduced two characteristic lengths: The coherence length ξ

as a measure of the size of thermodynamic fluctuations in the superconducting phase, and the penetration depth λ that describes the depth to which an external field can penetrate the superconductor. Unlike the two lengths, their ratio $\kappa = \lambda/\xi$ is independent from temperature and can be used to characterize the superconductor.

1.3 Superconducting devices

1.3.1 The Josephson junction

Two superconducting electrodes, separated by an insulating material, form a so-called Josephson junction. In 1962, Josephson predicted [10] that a zero voltage supercurrent should flow between the electrodes, depending on $\Delta\phi$, the phase difference between the phases of the Ginzburg-Landau-wavefunctions in the electrodes. This is called dc-Josephson effect:

$$I_s = I_c \, sin(\Delta\phi) \tag{1.2}$$

I_c is called the critical current and it is the maximal current the junction can support while staying in the superconductive state. Applying a constant voltage V across the junction causes the phase difference to evolve as

$$\frac{d(\Delta\phi)}{dt} = \frac{2eV}{\hbar} \tag{1.3}$$

This is the ac-Josephson effect. These two predictions were part of the work leading the Nobel Prize Committee to award Josephson half of the 1973's Nobel Prize [8] "for his theoretical predictions of the properties of a supercurrent through a tunnel barrier, in particular those phenomena which are generally known as the Josephson effects".
The Josephson effect has been confirmed in many different experimental circumstances in which two superconductors are coupled by a weak link that allows Cooper pairs to tunnel through. Recent research results extend the effect to the more general case of a weak link between two macroscopic wavefunctions, including to the observation of both ac and dc Josephson effect in a Bose-Einstein-condensate [11].
Unfortunately, the phase difference $\Delta\phi$ is not a gauge-invariant quantity, thus the current I_s cannot be determined in general. By introducing a gauge-invariant phase difference γ,

$$\gamma \equiv \Delta\phi - (2\pi/\Phi_0) \int \mathbf{A} \cdot d\mathbf{s} \tag{1.4}$$
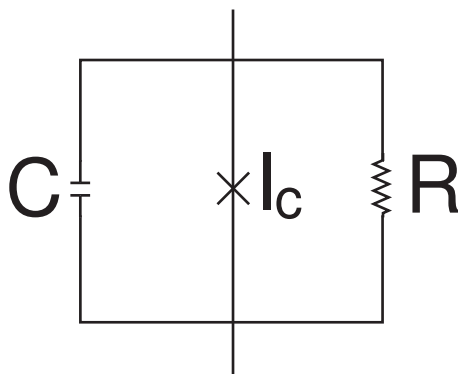
Figure 1.1: Sketch of the model for the physical Josephson junction: Ideal junction with critical current I_c, capacity C and resistance R in parallel.

the problem can be cured. The integration is from one electrode of the weak link to the other. This allows to express the supercurrent in an ideal Josepson junction in terms of γ, using Eq. 1.2 and replacing $\Delta\phi$:

$$I_s = I_c \, sin(\gamma) \tag{1.5}$$

This also allows the inclusion of magnetic field effects on the junction.

The RCSJ model

The resistively and capacitively shunted junction (RCSJ) model [9] provides a more complete description of the case of finite voltage across the junction. Its sketch is shown in Fig. 1.1. In this model, the physical Josephson junction is modeled by an ideal one with critical current I_c (see Eq. 1.5), shunted by a resistance R and a capacitance C. The resistance R takes account for the dissipation in the finite voltage regime, but does not effect the lossless dc regime. The capacitance C builds the geometric shunting capacitance between the two electrodes (not to ground!). The time dependence of the phase γ can be obtained by equating the bias current I to the total junction current from the three parallel channels:

$$I = I_{c0} \, sin(\gamma) + V/R + C \, dV/dt \tag{1.6}$$

The switch in notation from I_c to I_{c0} is anticipating that the observable critical current I_c might be less than the fluctuation-free intrinsic critical current I_{c0} of the RCSJ model. Later, and that is closely related to the experiment, thermal fluctuations will be treated.
For now, Eq. 1.6 can be rewritten by eliminating V in favor of γ using Eq.

4
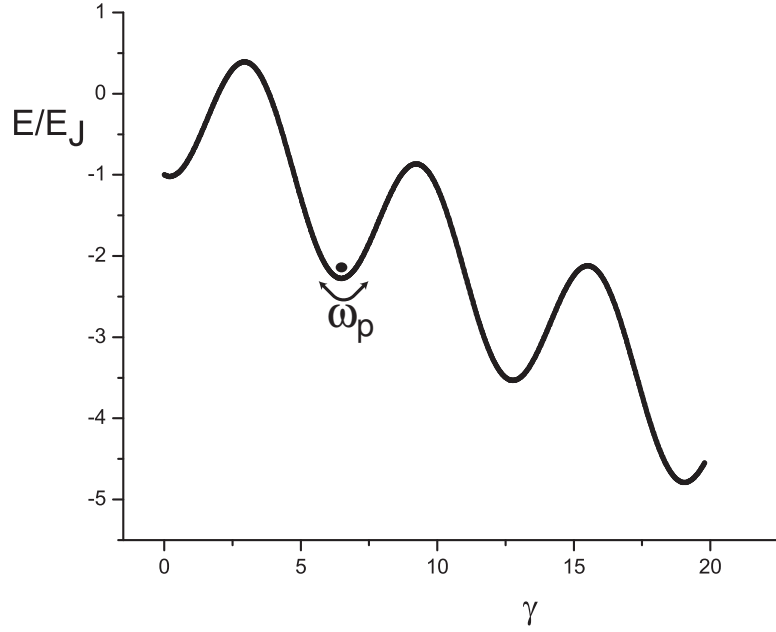
Figure 1.2: Tilted washboard potential of the physical Josephson junction according to the RCSJ model. The ratio of the currents T/I_{c0} was chosen to be 0.9. The fictitious particle oscillates in one potential well with the plasma frequency ω_p, but can switch to other wells by thermal activation or quantum tunneling.

1.3, and a second order differential equation is derived.

$$\frac{I}{I_{c0}} = \frac{d^2\gamma}{d\tau^2} + \frac{1}{Q}\frac{d\gamma}{d\tau} + sin(\gamma) \tag{1.7}$$

In this equation, a dimensionless time variable τ has been introduced, $\tau = \omega_p t$ with the so-called plasma frequency

$$\omega_p = \left(\frac{2eI_{c0}}{\hbar C}\right)^{\frac{1}{2}} \tag{1.8}$$

The "quality factor" Q is defined as

$$Q = \omega_p RC \tag{1.9}$$

Eq. 1.7 is similar to the equation of motion for a particle of mass $(\hbar/2e)^2 C$
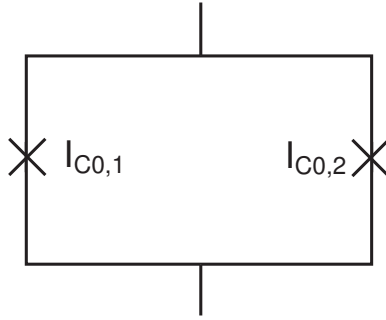
Figure 1.3: Sketch of the dc-SQUID. Two Josephson junctions in parallel are connected by superconducting electrodes

moving along the γ axis in an effective potential

$$U(\gamma) = -E_J cos(\gamma) - (\hbar I/2e)\gamma \tag{1.10}$$

Here, E_J is the Josephson coupling energy. The potential is shown in Fig. 1.2. For $I > I_{c0}$, there are no stable equilibrium points.

1.3.2 The dc-SQUID

Superconducting Quantum Interference Devices (or SQUIDs) are based on superconducting loops containing Josephson junctions. The current in the SQUID is dependent on the flux through it which makes SQUIDs widely used as precise magnetometers in a variety of applications. Two Josephson junctions connected by superconducting electrodes form a so-called dc-SQUID (See Fig 1.3). In this subsection, the effect of an applied magnetic field on the Josephson junctions is worked out. We have seen that the gauge-invariant phase across each junction depends on the magnetic vector potential **A** which is not gauge-invariant. It makes sense to give the results only in terms of the flux Φ through the area enclosed by the superconducting loop, since it is a gauge-invariant quantity. By integrating around the loop to determine the flux, the following expression for the phases is derived:

$$\gamma_1 - \gamma_2 = 2\pi\Phi/\Phi_0 \ (mod \ 2\pi) \tag{1.11}$$

As long as Φ is no integer multiple of Φ_0, the maximum supercurrent through the junctions must be less than the sum of the two single junctions, $I_m < I_{c0,1} + I_{c0,2}$. Assuming the junctions to be similar, $I_{c0,1} = I_{c0,2} = I_c$, and using the flux ϕ in units relative to $\Phi_0 = 2.07 \cdot 10^{-15}$ Wb, $\phi = \Phi/\Phi_0$, the maximum
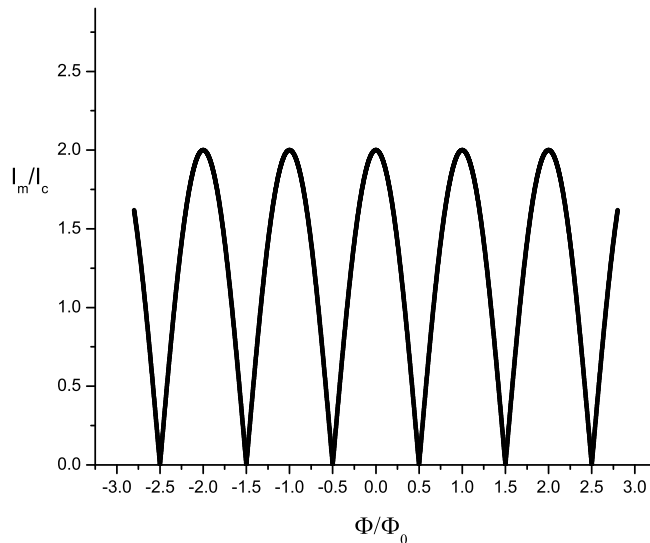
Figure 1.4: Maximal current of the dc-SQUID in dependence of relative flux $\phi = \Phi/\Phi_0$ through the junction.

supercurrent is given by

$$I_m = 2I_c|cos(\pi\phi)| \tag{1.12}$$

A plot of this relation is given in Fig. 1.4. This flux-dependence of the maximal current is the basis of using a dc-SQUID to measure small variations of the magnetic flux quantum Φ_0 (down to $5 \cdot 10^{-14}$ Gs within a few days of averaged measurements [12]).

A model of the dc-SQUID dynamics [1] consists of two ideal Josephson junction in parallel with capacitances C and connected by two inductances L_1 and L_2 in series. A sketch of this model is shown in Fig. 1.5. Although this is not used for the later treatment, we allow for some asymmetry in our analysis of the dc-SQUID: The loop is modeled using two inductances L_1, L_2 in series (total inductance L), with an asymmetry in these inductances given by $\eta = (L_2 - L_1)/L$. The asymmetry parameter for the critical current is α. The junctions have critical currents $I_0(1 - \alpha)$ and $I_0(1 + \alpha)$, and the circulating current is $J = (I_2 - I_1)/2$. Since the escape rate from one potential well is expected to depend only on the potential-barrier height and normal-mode frequencies, no source of damping or noise is inserted.
The equations of motion of the dc-SQUID are then similar to the equations of
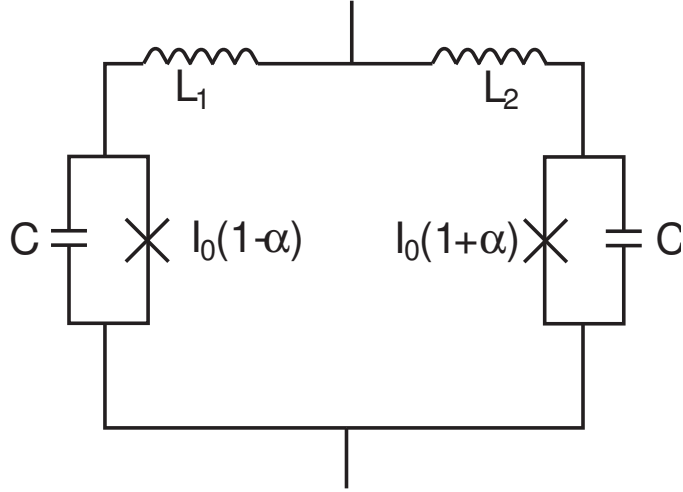
Figure 1.5: Model of the dc-SQUID ([1]): Two ideal junctions (asymmetric critical current $I_0(1 \pm \alpha)$ with capacitances C in parallel coupled by a superconducting ring with asymmetric inductances L_1 and L_2. Noise or damping sources have not been incorporated.

motion of a particle of mass C moving in a potential U:

$$U(\phi, \phi_{dc}) = \frac{1}{4\beta}(\phi - \phi_b)^2 - \frac{i_b}{2}\phi - cos(\frac{\phi_{dc}}{2})cos(\phi) - \alpha sin(\phi)sin(\phi_{dc}) - \frac{\eta i_b}{2} \quad (1.13)$$

The loop is biased by the normalized current i_b in units of $2I_0$ and the external flux ϕ_b in units of a flux quantum $\Phi_0/2\pi$. The junction's energy is $E_J = 2I_{c0}\Phi_0/2\pi$ and β is defined as $\beta = 2\pi L I_{c0}/\Phi_0$. A plot of the potential (assuming no asymmetry, $\eta = 0$, $\alpha = 0$) is provided in chapter 3 (Fig. 3.5). The mean slope along the ϕ direction is proportional to the bias current I. The curvature in the ϕ_{dc} direction is due the inductive coupling between the junctions depending on $1/(4\beta)$. The potential-barrier height between adjacent wells is determined both by the flux bias ϕ_b and the normalized bias current i_b. As i_b decreases, the barrier height decreases as well.

1.3.3 The rf-SQUID

As a simpler system, the rf-SQUID had been studied before the dc-SQUID. The rf-SQUID consists of a Josephson junction shorted by a superconducting loop. It is a system with only one quantum variable, given by the phase across the junction. Analogous to the scheme for the physical junction in Fig. 1.1, the rf-SQUID is modeled by adding an inductance representing the inductance
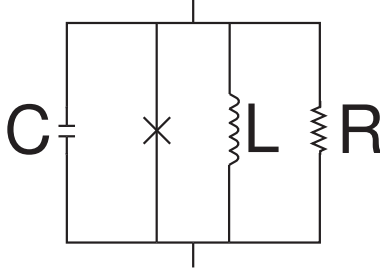
Figure 1.6: Sketch of the rf-SQUID. The Josephson junction is modeled according to the RCSJ model, and the inductance of the superconducting loop is added.

of the superconducting loop [13]. This scheme is shown in Fig. 1.6. In quasi-static approximation (low operation frequency), an applied flux changes the phase according to

$$\gamma = 2\pi\Phi/\Phi_0 \ (mod \ 2\pi) \tag{1.14}$$

which is essentially the same as Eq. 1.11.

The circulating current is $I_s = I_c \ sin(2\pi\Phi/\Phi_0)$, and the screened flux Φ in the loop must satisfy $\Phi_x = \Phi + LI_s$ [9].

Analogous to the dc-SQUID, a fictitious particle of kinetic energy $\frac{1}{2}C\dot{\phi}$ can be considered moving in a potential given by the difference between the loop's magnetic energy and the Josephson junction's coupling energy.

$$U(\varphi, \varphi_x) = U_0[\frac{1}{2}(\varphi - \varphi_x)^2 - \beta_L cos(\varphi)] \tag{1.15}$$

Here, $U_0 \equiv \Phi_0^2/4\pi^2 L$ and $\beta_L \equiv 2\pi LI_c/\Phi_0$. The variables φ and φ_x are Φ and Φ_x in units of $\Phi_0/2\pi$. The two local energy minima in this potential with respect to ϕ can only be obtained numerically:

$$\frac{dU(\varphi, \varphi_x)}{d\varphi} = 0 \ \Rightarrow \ \phi_{min} = \phi_x - \frac{\beta_L}{2\pi}sin(2\pi\phi_{min}) \tag{1.16}$$

This type of equation requires some kind of fixpoint approximation to give a solution. The two potential wells represent different fluxoid states of the rf-SQUID and correspond to currents circulating in opposite directions around the loop. For the current samples, these currents are about 3 μA.

9

1.3.4 The rf-SQUID as a qubit

In our group, the dynamics of rf-SQUIDs have been studied regarding their application as a qubit (quantum bit). For a better control of the experimental properties, it is very convenient to be able to adjust the barrier height of the potential independently of Φ_x. In the rf-SQUID, the barrier height is determined by the critical current of the Josephson junction and does not allow manipulation. However, by replacing the single junction by a very small dc-SQUID with inductance l, it is possible to influence the potential barrier as well. Applying flux to the small dc-loop will suppress the critical current, and therefore the barrier height will change. This addition will make the potential two-dimensional (depending on ϕ and ϕ_x), but under some conditions ($\beta_L << 1$ and $L >> l$), the potential can be treated as one-dimensional with small corrections [14, 15]. In Eq. 1.15, β_L has to be replaced by

$$\beta_L(\phi_{xdc}) = \beta_{L0}\, cos(\pi\phi_{xdc}) \tag{1.17}$$

where ϕ_{xdc} represents the external flux applied to the small dc-loop in units of Φ_0.

Without going too far into detail, the energy levels and wavefunctions can be calculated from the Hamiltonian, allowing for approximating the potential with the harmonic oscillator. D. Bennett [2] gives a detailed derivation since this method has been extensively used in his data analysis. For our purposes of fast diagnostics, no such careful analysis is necessary. It comes into play when a sample is considered good enough to be extensively studied, which is not part of this thesis.

For a quick overview, the Hamiltonian reads as ([16, 17])

$$H(\phi, \phi_x) = \frac{Q^2}{2C} + U(\phi, \phi_x) \tag{1.18}$$

with capacitance C and charge Q on the junction, the latter being a quantum conjugate variable to the phase across the junction and therefore to the flux through the loop ϕ. Following the physical picture of the energy oscillating between the inductance of the loop and the capacitance of the junction, and using the conjugation relation, the Hamiltonian can be rewritten similar to the harmonic oscillator plus a cosine term:

$$H = \frac{-\hbar^2}{2m}\frac{\partial^2}{\partial x^2} + \frac{1}{2}m\omega^2 x^2 - E_J cos\left[2\pi(x + x_0)\right] \tag{1.19}$$
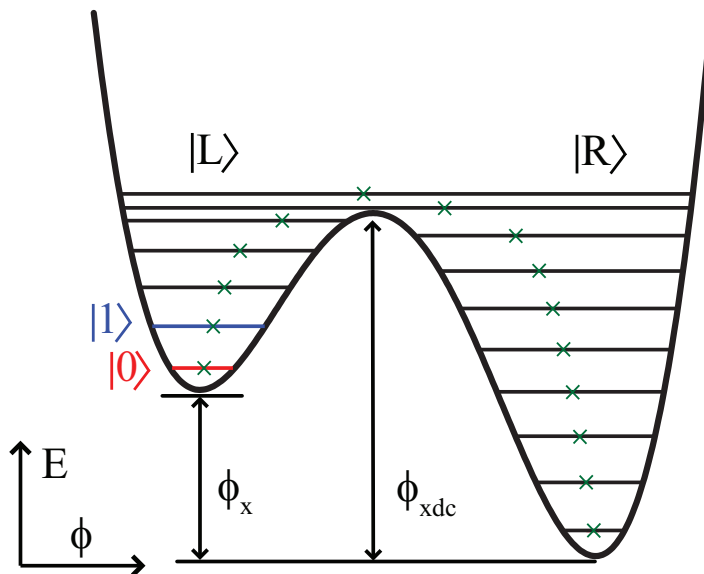
Figure 1.7: The potential of an rf-SQUID at $\beta = 1.32$ and $\phi_x = 0.507$ showing localized energy levels and the corresponding value of mean flux (green x), taken as is from [2].

In this equation, $m \equiv C\Phi_0^2$, $\omega^2 \equiv 1/LC$, $x = \phi - \phi_x$ and $x_0 \equiv \phi_x$. The cosine term can be expressed in terms of raising and lowering operators, and the resulting Hamiltonian is used to construct a matrix in the eigenstate basis of the harmonic oscillator. For numerical calculations of the first few levels, 70×70 is a sufficient matrix size. In [2], matrix sizes up to 200×200 have been used.

To give some idea about the energy levels, Fig. 1.7 shows the potential at $\phi_x = 0.507$ and for $\beta = 1.32$, and the corresponding values of mean flux. Levels below the barrier are in either one of the wells, but not aligned. Deep in the wells, the level are similar to the harmonic oscillator levels, but as the anharmonic term becomes more influential, the level spacing gets smaller.

1.4   Qubit design

A quantum two level system can form a so called quantum bit (qubit). Unlike a classical bit, quantum bit states include all superposition states of the classical bit states $|0\rangle$ and $|1\rangle$. The state of a qubit can be written as

$$|\Psi\rangle = \alpha |0\rangle + \beta |1\rangle, \tag{1.20}$$

11

holding $\alpha^2 + \beta^2 = 1$ for the complex coefficients α and β. The measurement of the qubit returns $|0\rangle$ or $|1\rangle$, with probabilities α^2 and β^2, respectively. The impossibility of measuring the state of the qubit with a single measurement is the key idea for all algorithms used in quantum computation. Suggested algorithms take advantage of the fast growing number of parameters (2^N) for N entangled qubits. This makes quantum systems hard to simulate on conventional computers. But for quantum computing algorithms, entangled computation paths with enhancement of the correct path via quantum interference allow to outperform conventional computers; and are expected to solve several problems that are today considered unsolvable such as to break the current RSA[1] encryption standard.

After the introduction of the main devices used in this work in the preceding sections, a few design goals and properties are to mention. Furthermore, a qubit for quantum computation has to hold the five DiVincenzo-criteria (DC) [18]:

1. Qubits have to be well defined, and the physical system has to be scalable.

2. There has to be the possibility to initialize the qubit in a certain state, at least $|000000...i\rangle$.

3. The system's decoherence time has to be sufficiently long (on a time scale given by the gate time).

4. A universal set of quantum gates has to exist.

5. The capability of measuring each specific qubit separately

The qubit chip fabricated in this group with $Nb/AlO_x/Nb$ junctions using Nb trilayer technologies allows for large-scale super-conducting circuit applications [19, 20] and gives also advantages since Nb junctions are more robust than Al junctions, unless the latter are stored under vacuum. Each choice of material and process will influence the quality of the samples, changing coherence times [2] or, as used as an indicator for sample quality in this research, the peak-to-valley ratio obtained in the escape rate measurent (See 4.2). [2] also gives a detailed overview over the fabrication process for the samples used in this thesis.

A scheme and a photograph of the qubit chip is shown in Fig. 1.8. The

---

[1]RSA is a encryption method relying on the impossibility to perform the prime factorization for a large number in sufficiently short time.
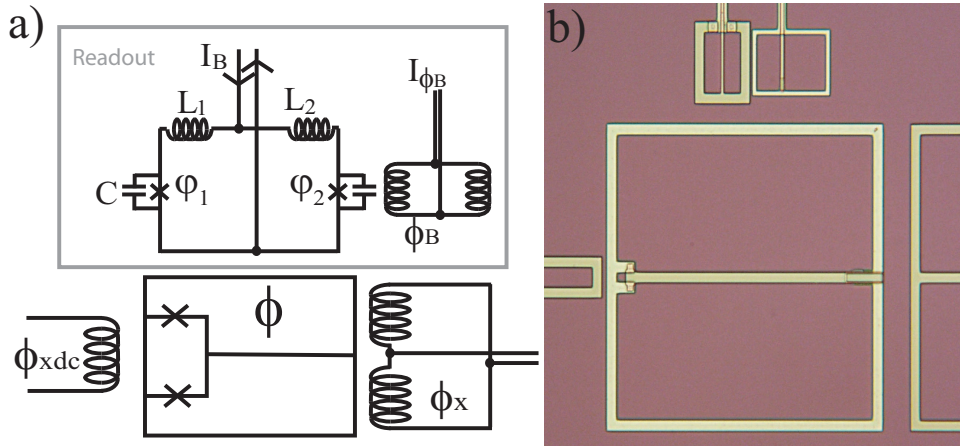
Figure 1.8: a) Schematic and b) photograph of rf SQUID qubit and the readout magnetometer. (from [2])

qubit loop is a square with side length 150 μm and a 5 μm wide trace. The dc-SQUID loop containing the junctions is 5 μm $\times$5 μm big. The inductances of the two loops have been calculated by D. Bennett [2] with the 3D-MLSI software package [21] to be $L \approx 215$ pH and $l \approx 10$ pH. The rf-SQUID loop is in the center and includes the dc-SQUID loop with the two junctions on the left side. The rf-SQUID is biased by the ϕ_x flux bias coil on the right side, and the potential barrier height for the dc-SQUID is changed by the ϕ_{xdc} flux bias coil. Above, the readout devices are shown. The magnetometer flux coil allows to couple the magnetometer bias flux ϕ_b to the dc-SQUID magnetometer, and the magnetometer itself is biased by the current I_b. The coupling of both ϕ_x and ϕ_{xdc} can be compensated by adjusting the magnetometer bias ϕ_b accordingly, since the ϕ_b bias coil is designed not to couple to the qubit. The magnetometer is also designed in a way that the current bias I_b does not couple to the qubit to first order. Therefore fluctuations in I_b and the whole readout process do not influence the qubit state. The mutual inductance between the qubit and the magnetometer has been measured to be 5 pH (design value 4.3 pH).

This design fulfills the DiVincenzo-criteria. The system is easily scalable, and each qubit can be manipulated and read out independently as shown. It is also possible to set each single qubit into one of his orthogonal states by tilting the potential. Applying flux in ϕ_x can force the system into one of the potential wells. The issue of sufficiently long coherence times has been studied [2]. Work is also currently in progress to probe different materials and processes in the fabrication. The work of this thesis helps to improve coherence times by allowing for fast sample diagnosis.

Chapter 2

Experimental Setup

The cryogenic setup for the experiments has been used for many years, thus the techniques used within this research are well known. The dilution refrigerator was suggested in the 1950's and built in the 60's, and evaporative cooling mechanism have been known for longer. These years also saw a surge of activity in the understanding of superconducting devices, as has been mentioned in the introduction chapter. For most of the time since then, this group has contributed to the continuous improvement of devices based on Josephson junctions.

2.1 Achieving low temperatures

Since the experiments related to this research are relying on superconducting devices, the experiment has to be performed at very low temperatures, usually below 1 K. The boiling point of liquid helium (mostly ^{4}He) is at 4.2 K (at normal pressure). As well known from thermodynamics, evaporative cooling can allow for lower temperatures than those achieved at atmospheric pressure. By pumping on ^{4}He, the temperature can drop to 1.2 K. By substituting the ^{4}He by its lighter isotope ^{3}He, even lower temperatures (down to 300 mK) can be achieved. The serious issue in reaching these temperatures is to keep the heat load as small as possible, both by assuring a good thermal insulation to the warmer parts of the system and by reducing the heat dissipation by the experiment as much as possible. This leads to the concept of the ^{3}He-cryostat.

Our ^{3}He-cryostat is used to measure the behavior of superconducting devices fabricated in this group at temperatures between 300 mK and 1.2 K. Since it does not circle the ^{3}He, it can only be run for a certain time, typically
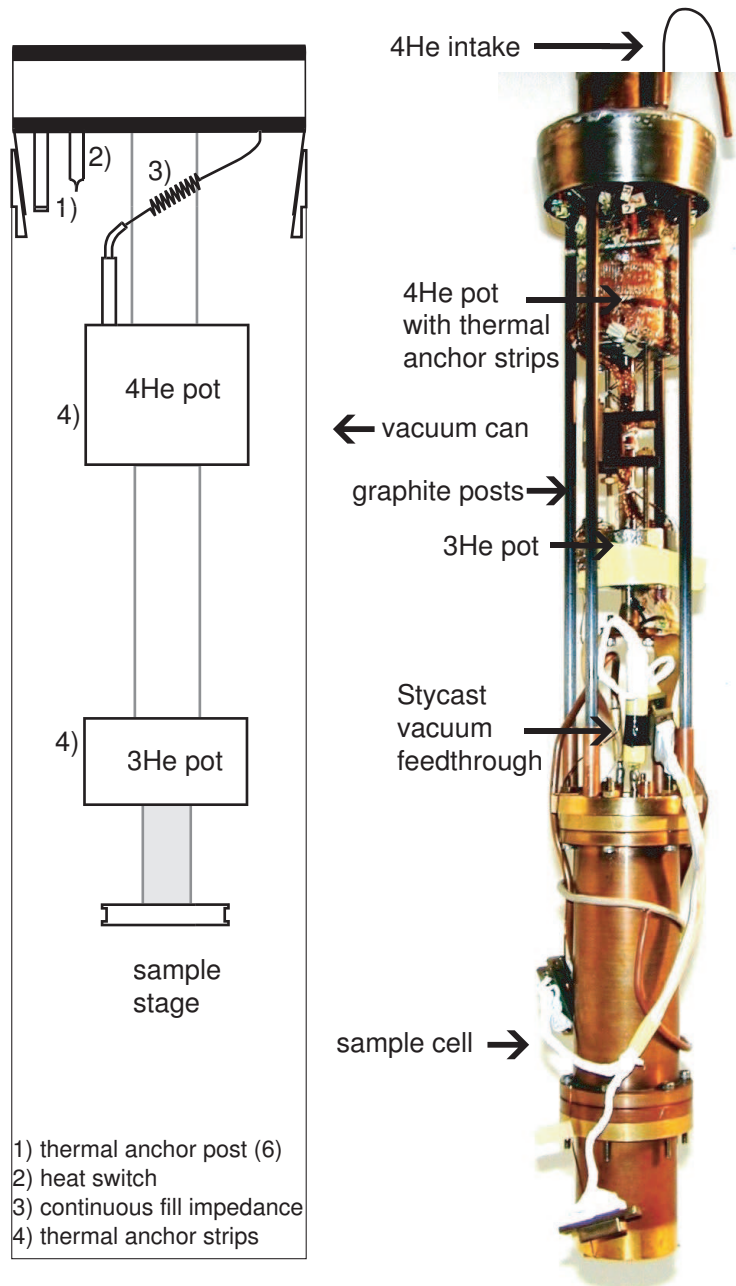
Figure 2.1: Schematic (left) and photograph (right) of the ^{3}He cryostat. Two gold plated copper strips provided thermal contact between the ^{3}He pot and the top and bottom of the sample cell.

between 6-10 hours, depending on the heat load.

Fig. 2.1 shows a schematic of the apparatus. The cryostat is immersed in liquid ^{4}He. The 1 K pot is filled with liquid ^{4}He which is constantly being pumped on. Its temperature goes typically down to 1.2 K. The 1 K pot is replenished through a small impedance that connects it with the surrounding bath. ^{3}He can be liquefied by flowing through the 1 K pot. The liquid ^{3}He is then collected in a ^{3}He pot. Since ^{3}He is very expensive, it is stored in an absorber and released when required. For this purpose, there is a heater that heats the absorber and releases the ^{3}He. When it comes in thermal contact with the 1 K pot, it is liquefied and drips down into the ^{3}He pot. At this stage a sorb pump is activated to pump on the ^{3}He pot and to achieve the instrument's base temperature.

2.1.1 Heating issues

The He3 fridge had previously been used for an experiment to study low-frequency noise in Josephson junctions [22]. This experiment required a smaller sample cell which could be directly attached to the sample stage in order to maximize its cooling performance. With respect to the previous experiment the sample cell used by us is more complex and heavier, therefore we choose to not have direct thermal contact between the ^{3}He pot and the sample cell as originally designed, since this might put too much mechanical stress on the ^{3}He line and the pot, which might then cause them to break. Therefore, using four posts, the sample cell has attached to the vacuum flange instead of the sample stage. A thermal connection has then been created between the sample stage and the cell using gold plated copper strips.

To reduce the heat load on the ^{3}He pot and the sample stage, some modifications have been made:

Rods had to be introduced to hold the sample can in place. To bring the thermal conductivity to a minimum, and still assure enough stability, graphite post were chosen. The heat transfer $\dot{Q}$ reads as [23]

$$\dot{Q} = 4\frac{A}{l} \int_{0.3\ K}^{4.2\ K} d\lambda\ \lambda(T), \tag{2.1}$$

since the four posts are anchored at 4.2 K (vacuum flange) and 0.3 K (^{3}He pot). $\lambda(T)$ is the temperature-dependent thermal conductivity of the solid. Since the heat transfer is proportional to the area of the post, we chose tubes rather than rods. To prevent heat flow through the wires down from room temperature, the wires are thermally anchored at each stage. The filters for the current lines are glued to brass thermal anchor posts that are screwed

16
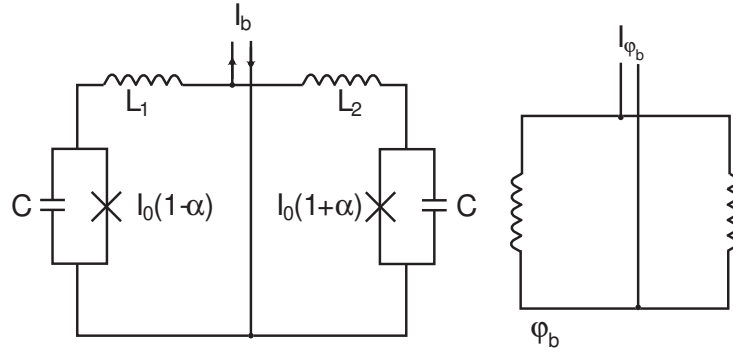
Figure 2.2: Schematic of the readout: Hysteretic dc-SQUID magnetometer (left) and magnetometer flux bias coil (right).

into the flange of the outer vacuum can. The wiring stage between the 1 K pot and the sample cell has been replaced, using superconducting wires rather than resistive wires. These are bad thermal conductors and do not cause any resistive heating.

After these improvements had taken place, a base temperature of 430 mK was achieved.

2.2 Switching current measurement

The state of the qubit can be sensed by measuring the switching current of the on-chip hysteric dc-SQUID magnetometer. The switching current is a function of flux through the SQUID loop. Since the qubit is inductively coupled to the magnetometer, a change in flux corresponds to a change in switching current. By using the optimal bias for the magnetometer, low back action can be achieved (no inductive coupling to first order) which allows one to read out the qubit flux state before induced fluctuations can destroy quantum coherence [2]. Fig. 2.2 shows the readout mechanism, consisting of the magnetometer and the ϕ_b coil. The magnetometer is designed with junctions asymmetric in size and therefore in critical current to shift the minimal magnetometer back action point closer to the switching current of the magnetometer.

The magnetometer bias current is ramped from 0 to some value higher than the switching current I_{sw}. At the switching current I_{sw}, the voltage goes from zero to some finite value.

With the fast diagnosis setup, a LabView program running a NI-DAQ card was used. The DAQ card was used to send the qubit flux bias ϕ_x pulses and to give the ϕ_{xdc} level in two of the analog output channels. The trigger

channel was used to trigger the magnetometer current ramp which is sent by a Stanford Research Systems DS 345 function generator. By having all signals coming from the same device, perfect synchronization could be assured. The readout for the switching current of the magnetometer is done by the analog input channel of the DAQ card. Constant ϕ_b voltage is applied from an isolated voltage source. The magnetometer bias current is sent from a Stanford Research Systems DS 345 function generator. It goes through an isolation amplifier and a bias box, which consists of sensing and biasing resistors. The biasing resistor is meant to limit the current being applied, and the current is monitored over the sensing resistor. When the trigger box, a voltage threshold detector, reads a voltage higher than the threshold, it sends out a trigger pulse to the DAQ which reads the switching current.

2.2.1 The LabVIEW data acquisition program

The measurement process is controlled by a LabVIEW[1] program. Fig. 2.3 shows its central part. Depending upon the requirements of the specific measurements, this central part may be surrounded by other loops to step one or multiple biases. The configuration here is used to obtain switching current distributions for escape rate measurements, stepping the level of the trapezoid ϕ_x pulse (see also Fig. 2.8 for the waveforms in the escape rate measurement). The individually adjustable waveform parameters are send to a sub-VI[2] that initializes the NI-DAQ card with the defined waveform parameters. The measurement sub-VI is inside a while loop that repeats the measurement as often as required for a certain ϕ_x value, controlling the waveforms as described above. The 2-level measurement stack provides an adjustable time delay after each measurement allowing the qubit to relax. The measured switching currents are stored in an array that is processed for analysis in the case of the escape rate measurement (using the deconvolution part of the program described in Sec. 3.4) and saved otherwise. The end-DAQ-VI closes the channels, so that the new waveforms can be loaded.

The initial measurements in the next section use the same scheme, but instead of having a trapezoid pulse that is stepped, the general offset is changed. Hence, only the initialization sub-VI is slightly different in this case. The surrounding loop averages then over all switching events for one bias value.

---

[1]LabVIEW (short for Laboratory Virtual Instrumentation Engineering Workbench), from National Instruments, is a development environment for a visual programming language named G.

[2]LabVIEW programs are called virtual instruments (VI), hence VIs used as subprograms are called sub-VIs.
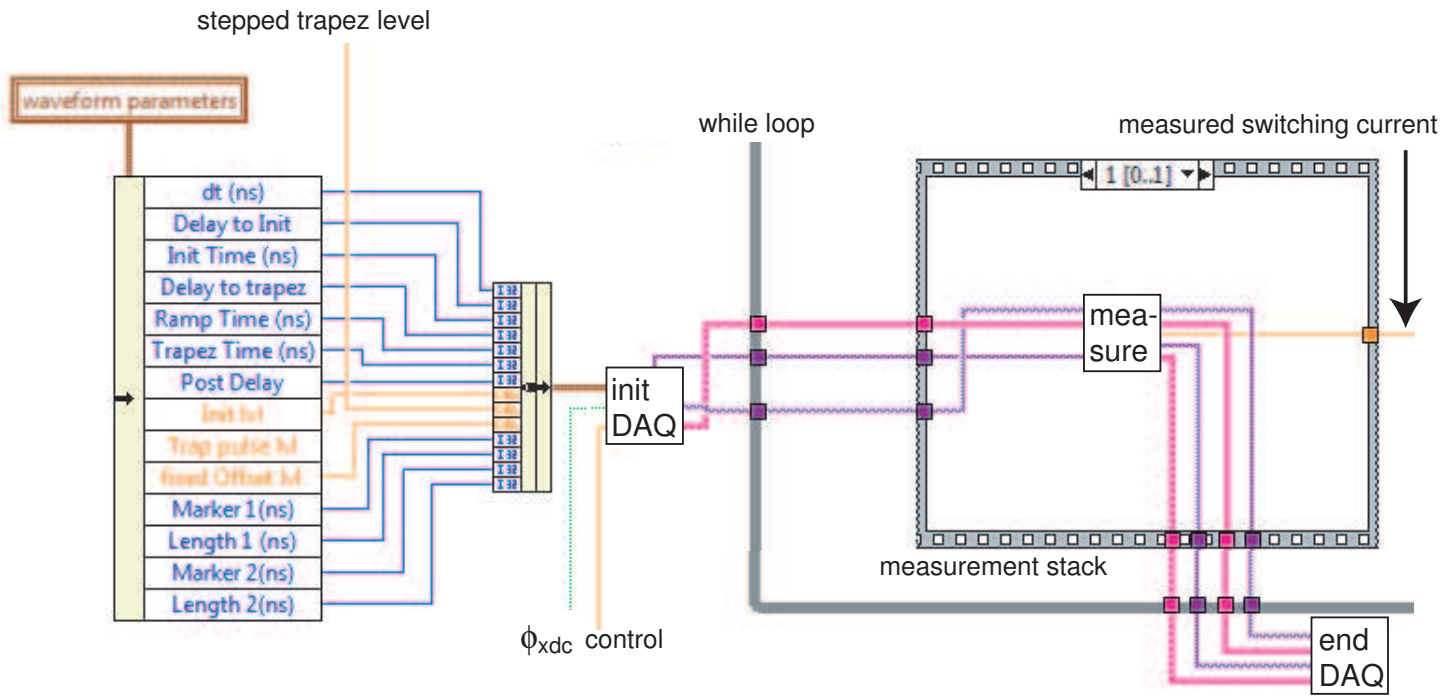
Figure 2.3: Scheme of the measurement conducing part from the LabView program designed to measure escape rates.

19

2.3 Initial measurements and calibration

For the measurements described later this chapter, like escape rate measurements, a careful calibration from current to flux is necessary. Furthermore, these measurements are used to assure complete functionality of the coils used for each particular measurement. They are also used to obtain information about some parameters of the qubit chip. The initial measurements usually include

- Measurement of the magnetometer switching current as a function of flux bias ϕ_b (ϕ_b calibration)

- Measurement of the hysteresis loop to determine the ϕ_x calibration (ϕ_{xdc} fixed)

- Measurement of the hysteresis loop size as a function of ϕ_{xdc} to determine β_{L0} and to calibrate ϕ_{xdc}

2.3.1 Magnetometer switching current as a function of flux bias

A measurement of the magnetometer switching current as a function of flux bias ϕ_b is usually the first initial measurement, and it is referred to as a "transfer function" measurement. The positions of the maximums give a value for the current corresponding to one flux quantum in ϕ_b, since the period of the transfer function is exactly one flux quantum. Fig. 2.4 shows such a measurement. For the linear portion of this function, the switching current of the magnetometer is proportional to the flux through the dc SQUID loop of the magnetometer and therefore to the flux change in the qubit. The measurement is also required to decide upon where to "park" the magnetometer, *e. g.* choosing an offset value for ϕ_b which should be positioned in the linear part of the transfer function. As the slopes on the two sides of the maximum differ[3], it is preferred to choose a ϕ_b value on the steeper side of the transfer function, since this increases the separation of the magnetometer switching distributions corresponding to different fluxoid states. The chosen ϕ_b value should also assure low back action between magnetometer and qubit.

---

[3]This effect becomes stronger as the temperature decreases; even showing a discontinuity in the minimum for very low temperatures.
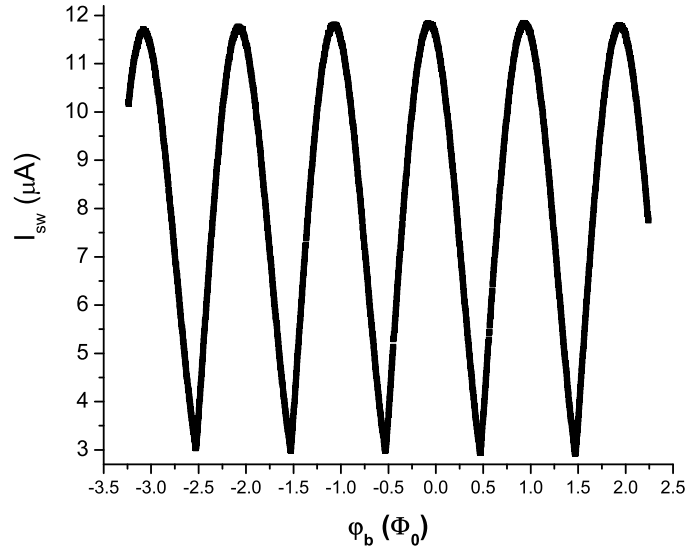
Figure 2.4: The measured mean switching current of the magnetometer at 600 mK as function of flux applied from ϕ_b

2.3.2 Measuring flux in the qubit

For all the measurements, it is required to know the quantum state in which the qubit is. The flux is the mascroscopic observable that corresponds to the quantum mechanical state. The total flux in the loop of the rf-SQUID reads as [24]

$$\phi = \phi_x - \beta_L \, sin(\phi) \qquad (2.2)$$

For $\beta_L = 2$, which is close to the value determined from the measurement, the total flux ϕ is plotted in Fig. 2.5 as a function of the external flux ϕ_x applied to the qubit. For some values of the external flux, there are three possible values for the total flux. The branch with the negative slope is unstable, but the other two branches are both possible. Depending of the history of the qubit, either one will be chosen. The jump to the other state occurs then roughly at the point and in the direction the arrows indicate in the figure. This gives hysteresis loops. Their size depends on β_L and therefore on the temperature and ϕ_{xdc} as given in chapter 1, Eq. 1.17. A measurement of the mean switching current I_{sw} (averaging typically over 20-40 counts per point, depending on the required precision) in the magnetometer is shown in Fig. 2.6. It shows the hysteresis loop as expected from the theoretical graph 2.5. The measured average switching current is proportional to the flux in the qubit since the

21
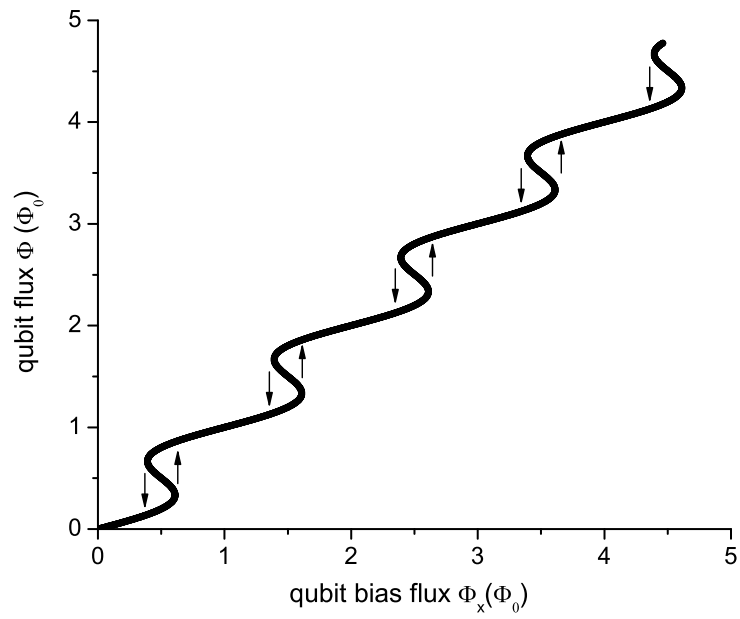
Figure 2.5: Qubit flux Φ as a function of qubit bias flux Φ_x in units of Φ_0 calculated using Eq. 2.2 and $\beta_L = 2$. Since the parts with negative slope are unstable, hysteric flux loops occur roughly along the arrows.
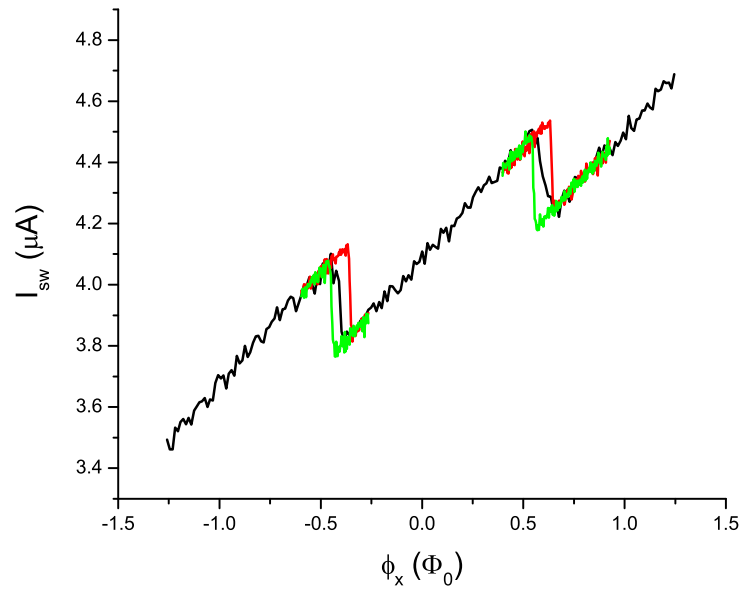
Figure 2.6: The measured mean switching current of the magnetometer as function of qubit bias flux ϕ_x. The black line (20 averaged measurements/point) has no initialization, for the red (green) line (40 av./pt.) initialization to the left (right) has taken place.
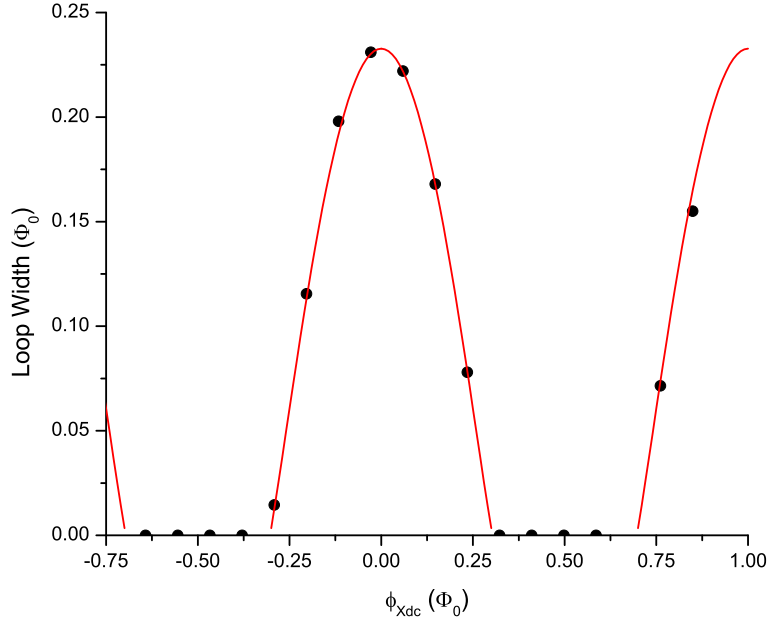
Figure 2.7: From [2]: The measured width (black circles) of the hysteresis loop of the qubit as a function of flux from the ϕ_{xdc} bias loop along with the calculated width (red line) for $\beta_{L0} = 2.29$ and $\Delta U = 5.4\ K$.

magnetometer was operated in the linear part of the transfer function. For this measurement, the bias flux for the ϕ_{xdc} coil was kept constant. The flux sent in the ϕ_x coil was used to initialize the qubit with a $1\ ms$ pulse in one well, and then the general offset level was stepped. The chosen qubit's potential well determines which branch of the hysteresis loop is being measured. For the other branch, ϕ_x is pulsed the other way, e.g. the pulses are added with the opposite sign to the general offset. For the case of no initialization (black line), a superposition of the two states is obtained.

The distance between two loops corresponds to one flux quantum in ϕ_x. This property is used to calibrate the current sent in the ϕ_x line.

As a next step, the same measurement is repeated for different ϕ_{xdc} biases. Since β_L depends on ϕ_{xdc} (Eq. 1.17), this changes the size of the hysteresis loop. A typical measurement is shown in Fig. 2.7 which is taken from [2] without alterations. It allows one to calibrate the current in the ϕ_{xdc} line, since one period equals one flux quantum. The fit used for this data led to $\beta_{L0} = 2.29$. This value was obtained under the assumption that the timing of the waveform does not change during the measurement of the different widths, and that the fluxoid state of the qubit switches on average from the metastable state to the other state at the same barrier height. The barrier height has been

estimated to be $\Delta U = 5.4\ K$.

Additionally, the measurements of the hysteresis loop can be used to obtain information about the cross coupling between the flux bias coils. This cross coupling has be compensated for by adjusting the magnetometer flux bias ϕ_b accordingly.

2.4   Escape rate measurement

The measurement of escape rates from one potential well to the other brings together all the ideas treated in this chapter so far. With all calibrations it is now possible to measure the dynamics of the qubit. In the beginning of the measurement, the qubit is in a metastable state in one well. This state is not the ground state of the system, but the ground state within a given potential well. Then the qubit flux bias ϕ_x is pulsed for a certain time t_m to allow the state to hop over the barrier (thermal escape) or tunnel through it (quantum regime), depending on the temperature of the experiment. If the state which the system tunnels into relaxes fast enough to the ground state of the well, than the system will remain in the new flux state which can then be read out.

The constant current in ϕ_{xdc} allows for adjusting the barrier height. As described above, the ϕ_b level is set to a certain value ("parked magnetometer"). The general level of the current applied on the qubit flux bias ϕ_x is chosen to tilt the potential to a position where the qubit is in a superposition of both states. Additionally, the initialization and the measurement pulse are applied. First, the initialization pulse makes sure the qubit is in the metastable state. The measurement pulse than tilts the potential such that there is a possibility for thermal (or quantum, depending on the temperature) escape of the quasiparticle in the other well. Fig. 2.8 shows a cartoon of the waveforms used in this measurement, and from Fig. 2.9, the resulting change in the qubit potential becomes obvious.

The theory of thermal escape from a potential well will be treated in the next chapter, especially focusing on finding a way to analyze the data already in the data acquisition program.
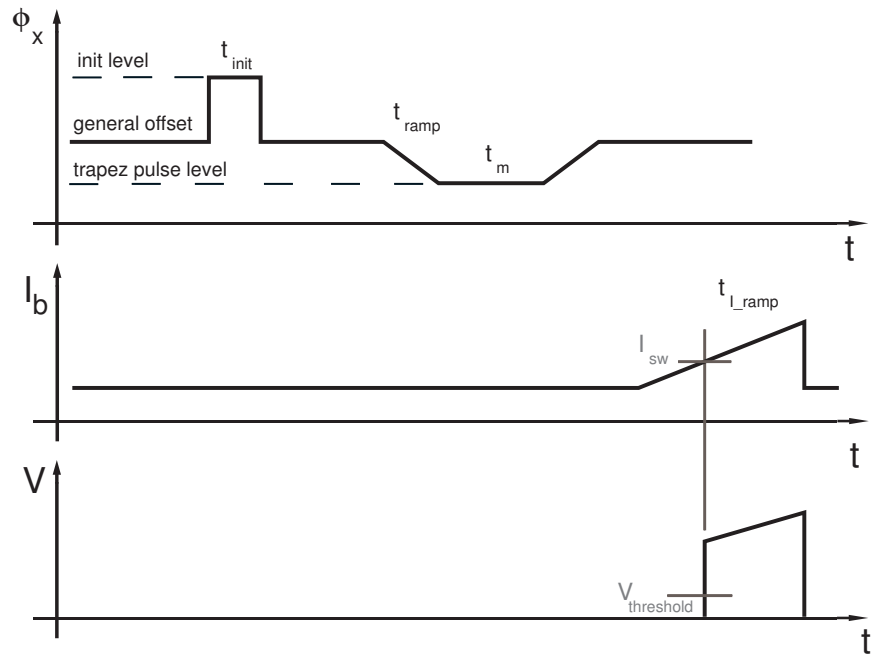
Figure 2.8: Waveforms sent in the qubit flux bias ϕ_x and in the magnetometer bias current I_b. At the switching current I_{sw}, the the magnetometer switches from the zero-voltage state to a finite-voltage state above the threshold level, triggering the DAQ to read the actual bias current value as switching current.
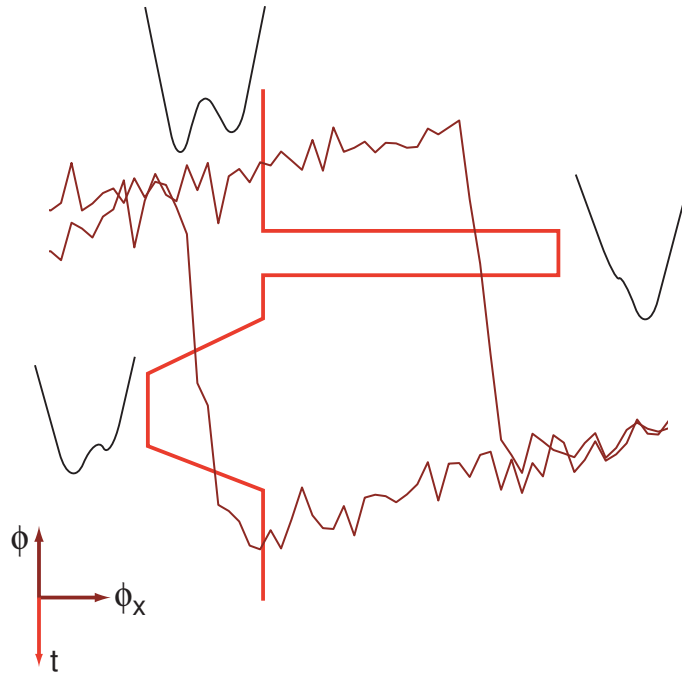
Figure 2.9: Measured hysteresis loop and scheme of the sent waveform in the ϕ_x bias. X-axis represents ϕ_x, the y-axis is switching current for the loop (proportional to ϕ) and time for the waveform (increasing in negative direction). Cartoons of the potential at different points of applied flux have been added.

Chapter 3

Deconvoluting switching current histograms

One of the main goals of the research related to this thesis has been to use the knowledge about switching current histogram statistics to analyze data in the high temperature regime (up to 1.3 K). Whereas the distinction between the two fluxoid states in the lower temperature regime, where the distributions are more separated, is just done by setting a threshold level, this method fails for higher temperatures as the distributions are broader and begin to overlap. By using the theory presented in this chapter to fit the data while running the measurement, it provides a tool to carefully measure escape rates over a wider range of temperatures. It also allows one to access a broader part of the transition for the rate measurement at temperatures where the threshold method starts to fail, as will be discussed in Sec. 4.5 in the next chapter.

The possibility to measure escape rates at temperatures between 1.3 K and 500 mK allows for a quick turnaround time in qubit sample diagnostic experiments. Generally, for all experiments related to that thesis research, temperatures were higher than the cross-over temperature, however the presence of quantum tunneling from an excited state can be observed.

The experiment explained in Sect. 2.4 gives as a result some distribution of switching current values. A typical measurement is shown in Fig. 3.1. The distribution is clearly not Gaussian since it is asymmetric. With the theory presented in this chapter, it is possible to derive an analytical formula that allows fast calculation of switching current distribution. The later derived formula 3.11 is used in Fig. 3.2 to simulate switching current events. The calculated events seem to be in good agreement with the experiment.
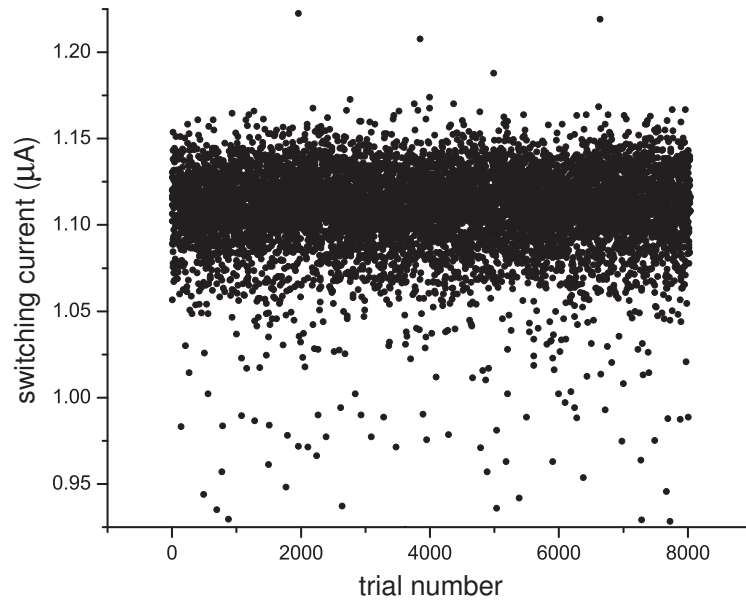
Figure 3.1: The switching current for 8,000 switching events, measured in a ^{3}He-cryostat at 530 mK.
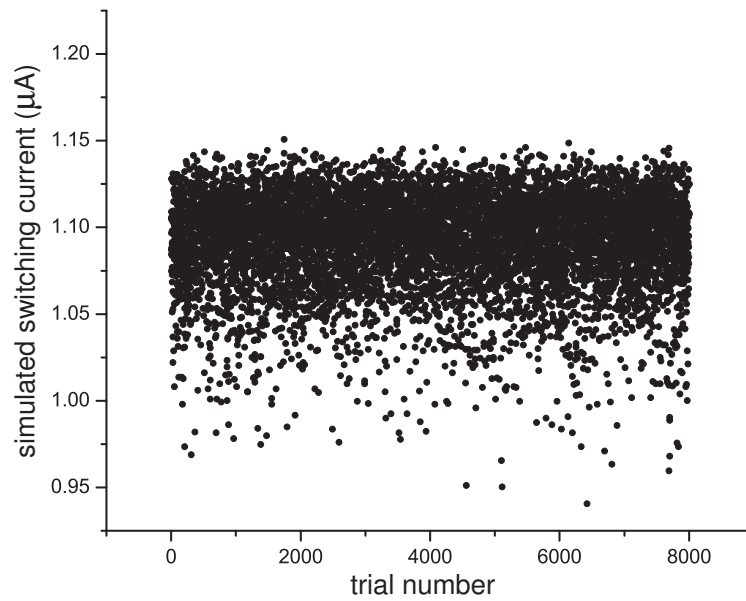
Figure 3.2: The calculated switching current for 8,000 switching events, simulated with the model with the linearized exponent. The width and the mean of the switching current distribution are arbitrary, but are chosen to be comparable to the measured data in Fig. 3.1.

3.1 Escape rates for a single Josephson junction and the rf-SQUID

It is useful to begin our discussion with the theory of escape rates for a Josephson junction (JJ). Under the conditions typical for our experiments, the formula for escape rates for the 2D-dc-SQUID potential has a similar behavior to that of a single Josephson junction. The theory of the noise-activated escape from a potential well into another well has been widely studied. In a seminal paper, H.A. Kramers [25] discussed the general case of Brownian motion in a field of force. This work has been extended later for the case of Josephson junctions by Kurkijärvi [26], Büttiker, Harris, Landauer [27] and others [28, 29].

Kramers found that the thermal escape rate has the simple form of the Arrhenius law:

$$\Gamma = a_t \frac{\omega}{2\pi} e^{-\frac{\Delta U}{k_b T}} \tag{3.1}$$

In this equation, ω is the frequency of small oscillations at the bottom of the 1D potential well, a_t is a damping factor (less than unity), ΔU is the height of the potential barrier, k_B is the Boltzmann factor and T the absolute temperature. For currents less than the critical current, the zero-voltage state is metastable and there is some switching probability. The potential barrier height given by [3, 28]

$$\Delta U = 2U_0 \left(\left[1 - \left(\frac{I}{I_c} \right)^2 \right]^{\frac{1}{2}} - \frac{I}{I_c} cos^{-1} \left(\frac{I}{I_c} \right) \right), \ I < I_c$$

$$\cong \frac{4\sqrt{2}}{3} U_0 \left(1 - \frac{I}{I_c} \right)^{\frac{3}{2}}, \ \left[\frac{I_c - I}{I_c} << 1 \right] \tag{3.2}$$

where $U_0 = I_0 \Phi_0 / 2\pi$. The potential can be considered to be cubic for $\frac{I_c - I}{I_c} << 1$.

The fit in Fig. 3.3 shows that the experimental data agree with the model used in the paper of Martinis et al. [3], which gives a first hint that, although we measured the histogram as the switching of a dc-SQUID, the theory for the Josephson junction and related approximations might work for the dc-SQUID magnetometer as well. The switching probability shown in Fig. 3.3 is related
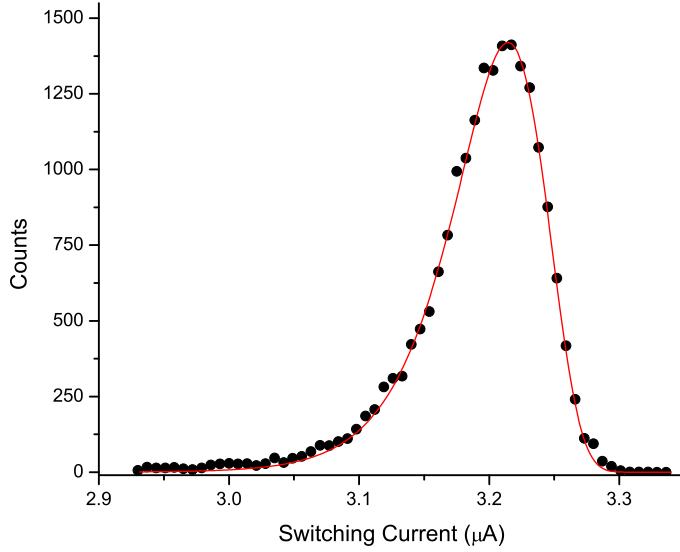
Figure 3.3: A measured histogram, fitted with the model for the Josephson junction [3]. When normalized, this curve represents a probability distribution for our dc-SQUID.

to the escape rate by the following relation:

$$P(I) = -\frac{d}{d\phi_x} exp\left[-\frac{1}{\dot{\phi}_x}\int_{-\infty}^{\phi_x} d\phi'_x \, \Gamma(\phi'_x)\right] \tag{3.3}$$

This expression allows one to calculate P(I) in a closed form if Γ is simple enough, but is usually non-analytical and therefore not very useful for the purpose of a real time fit in our data acquisition program. A first step toward an analytic approximation for the switching distribution was done by Kurkijärvi's [26] studies of the rf-SQUID, looking at the distribution in the external flux at which the ring admits a quantum of flux. He also considered the barrier height ΔU proportional to $(\Delta\phi_x)^{\frac{3}{2}}$, whereas the equilibrium Gibb's energy is linear in $\Delta\phi_x$.

$\Delta\phi_x$ is defined as $\Delta\phi_x := \phi_{xc} - \phi_x$, where ϕ_{xc} is the critical external flux at which a flux quantum enters the ring in the absence of fluctuations, and ϕ_x is the external applied flux. This leads to the following equation for the probability that a decay has not taken place:

$$W(u) = exp(-Xe^{-u^{\frac{3}{2}}}) \tag{3.4}$$

31

Here,

$$u = (U_0/k_bT)^{2/3}\Delta\phi_x$$

$$X = \frac{2}{3\dot{\Delta\phi}_x}\frac{\omega_0^2}{2\pi\eta}\left(\frac{k_bT}{U_0}\right)$$

(3.5)

W is related to the escape rate Γ by

$$W(t) = exp\left(-\int_{-\infty}^{t} ds\ \Gamma(\Delta\phi_x(s))\right)$$ (3.6)

and Eq. 3.4 follows after assuming the flux sweep to be linear in time and carrying out the integral.

The influence of the time-scale setting part $\frac{\omega_0^2}{2\pi\eta}$ depends on the dampening. η is defined as $\eta = 1/RC$, R and C are as introduced in Sec. 1.3.3. The barrier escape treatment is accurate as long as the sweep rate does not begin to compete with the factor $\frac{\omega_0^2}{2\pi\eta}$ (Still [26]). Under this conditions, Kurkijärvi derived the following analytical form the distribution $P(u) = dW(u)/du$:

$$P(u) = \frac{dW(u)}{du} = \frac{3}{2}X\sqrt{u}\ exp(-u^{\frac{3}{2}} - Xe^{-u^{\frac{3}{2}}})$$ (3.7)

Figure 3.4 shows the dependence of the shape of the distribution $dW(u)/du$ for different values of X. It is easy to see that for rising X the absolute value of the maximum and the corresponding u_{max} rise, and the width is getting smaller. It is worth mentioning here that the X-value influences width, position and amplitude of the histogram. This is important as we later intend to find a better fitting function for the switching current histogram, such that the different properties (width and mean) can be modulated by parameters independent from each other.

3.2 Escape rates for the dc-SQUID

A dc-SQUID magnetometer is the system of main interest for this work. Although the theory of escape rates has many similarities with that of the Josephson junction, the main difference is that the dc-SQUID is a quantum system with two macroscopic variables: δ_1 and δ_2, the two phases across the junctions in the dc-SQUID. The dynamics of the dc-SQUID can be treated as
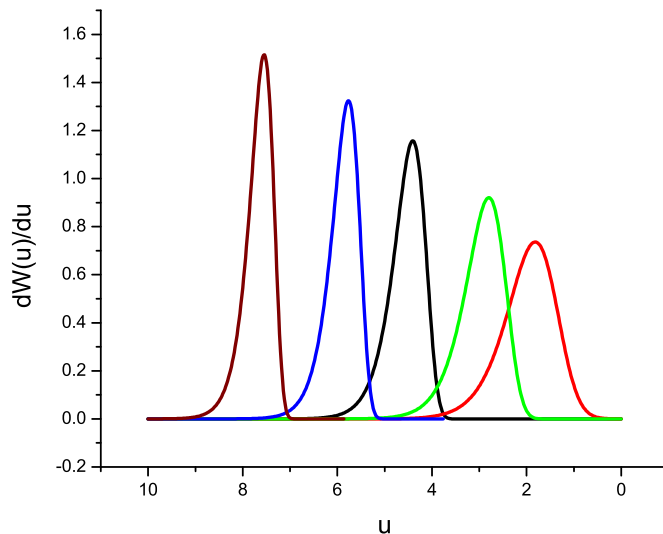
Figure 3.4: The distribution $dW(u)/du$ for different values of X. From left to right: $X = 10^9, 10^6, 10^4, 10^2, 10$.

a fictitious particle of mass C moving in a 2D potential [1, 30]. The potential can be written as

$$U(\phi, \phi_{dc}) = E_j \left(-cos\left(\frac{\phi_{dc}}{2}\right) cos(\phi) - x\phi + \frac{\beta_T j^2}{4} \right) \qquad (3.8)$$

The variables ϕ and ϕ_{dc} replace the two phases across the junctions δ_1 and δ_2. $\phi = (\delta_1 + \delta_2)/2$ is the average phase, and $\phi_{dc} = \delta_2 - \delta_1$ is the phase difference across the dc-SQUID. $j = (\phi_{dc} - 2\pi\phi_b)/\beta_T$ is the normalized circulating current, $x = I/2I_0$, and $\beta_T = 2\pi L I_0/\Phi_0$, assuming no asymmetry in the junctions and the loop (see Sec. 1.3.2).

Fig. 3.5 shows a 3D plot of the dc-SQUID potential as a function of ϕ and ϕ_{dc}. In the ϕ direction, the potential (without flux bias) shows a sequence of minima and saddle points. With $\phi_{dc} = 0$, this is exactly the washboard potential treated in the previous section. As $|\phi_{dc}|$ increases, the potential rises sharply. Thus, a particle trapped in a potential well would escape over the saddle point, e.g. near $\phi_{dc} = 0$.

In the thermal regime for temperatures well above the crossover temperature, the escape is similar to the one treated before. Kramer's formula 3.1 still holds, except that the oscillation frequency at the bottom of the well (ω_{lw}) is rescaled by the ratio of the transverse oscillation frequencies in the well (ω_{tw})

33
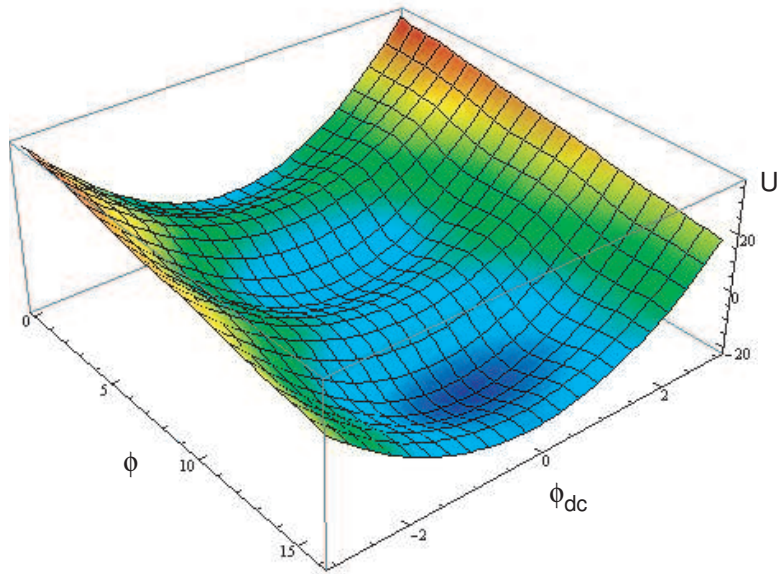
Figure 3.5: The potential for the dc-SQUID with zero flux bias ($\Phi_b = 0$) and $\beta_T = 0.3$. The potential shows a sequence of saddle points and local minima located at $\phi_{dc} = 0$ in the ϕ direction and rises sharply in the ϕ_{dc} direction as $|\phi_{dc}|$ increases.

and at the saddle (ω_{ts}). The escape rate then reads as

$$\Gamma = \frac{1}{2\pi}\omega_{lw}\frac{\omega_{tw}}{\omega_{ts}}a_t \; exp\left(-\frac{\Delta U}{k_bT}\right) \tag{3.9}$$

The minimum barrier height ΔU is reached at the saddle, T is the temperature and a_t is a damping dependent factor. Eq. 3.9 is equivalent to the thermal activation rate of a 1-D system having the frequency of small oscillations renormalized by ω_{tw}/ω_{ts} [30]. It is easy to show that the barrier height for a magnetometer is proportional to the current in the same way it is for the single Josephson junction: $\Delta U \propto (\Delta I)^{\frac{3}{2}}$. Thus, the mathematical treatment stays the same for both.

3.3 The probability distribution in linear approximation

A closer study of the distribution 3.7 will yield that the precise form of the distribution $P(u)$ is often not relevant. Thus, effort has been taken to find an analytic formula that allows one to get around the complicated and time-consuming numerical calculations. This has been successfully achieved for the rf-SQUID switching distribution [31, 32]:
If the exponent of the rate in Eq. 3.3 is slowly varying in the vicinity of some ΔI, then the barrier height dependence on I can be assumed to be linear and the rate can be approximated by

$$\Gamma = A \; exp(-B \; \Delta I) \tag{3.10}$$

In this equation, $B = \frac{\partial ln\Gamma}{\partial I}|_{\overline{\Delta I}}$ and $A = \Gamma \; exp(B \; \Delta I)|_{\overline{\Delta I}}$. Then, the regular distribution function follows to be

$$P(u) = X \cdot e^{-u-X\cdot e^{-u}} \tag{3.11}$$

where $X = A/\dot{I}B$ and $u = B \; \Delta I$.

X determines the maximum and, as we will see, the mean of the distribution ($u_{max} = ln(X)$) and u includes the scaling factor between switching current and width of the distribution. In the more general, not normalized case, an amplitude factor A is added.
The moments of this distribution have been calculated previously [31] and have been found to be (where γ is Euler's constant and $\zeta(s)$ is Riemann's Zeta
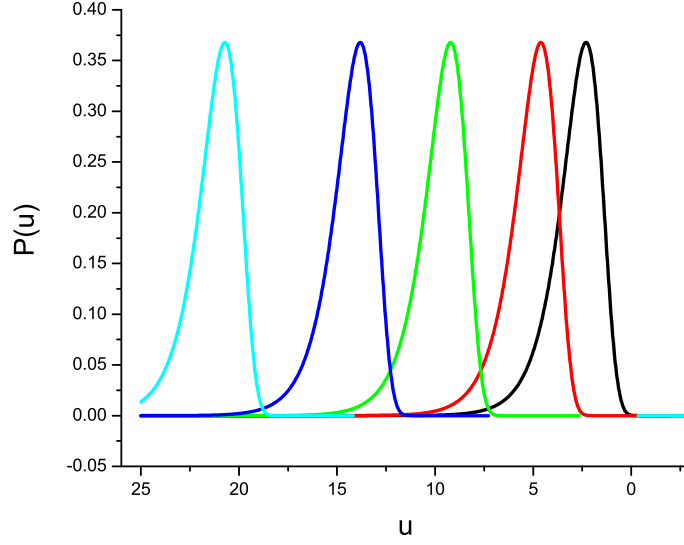
Figure 3.6: Comparison between the fitting functions in linear approximation for (from left to right) $X = 10^9, 10^6, 10^4, 100, 10$. Width and amplitude are independent from X. Amplitude A was set to 1.

function):

$$< u >= \gamma + ln(X) \approx 0.557216 + ln(X)$$
$$\sigma_u =< (u- < u >)^2 >= \frac{\pi^2}{6} \approx 1.64493$$
$$< (u- < u >)^3 >= 2 \cdot \zeta(3) \approx 2.40411$$

$$(3.12)$$

The moments 3.12 and the figure 3.6 show the independence of the shape of the distribution from the variable u and the parameter X. X only determines the position of the mean and the maximum of the distribution. The amplitude only depends on the amplitude factor A. By factoring u in a scaling factor and current I for a more convenient analysis of the data, we see that the width is only determined by the value of the scaling factor.

Comparing the fits in 3.3 and 3.7, the first done using the theory for the underdamped junction [3], the latter using the derived analytic expression in Eq. 3.11, both seem to work equally well for our case. Thus, this formula was found to hold also for the dc-SQUID magnetometer and to give surprisingly
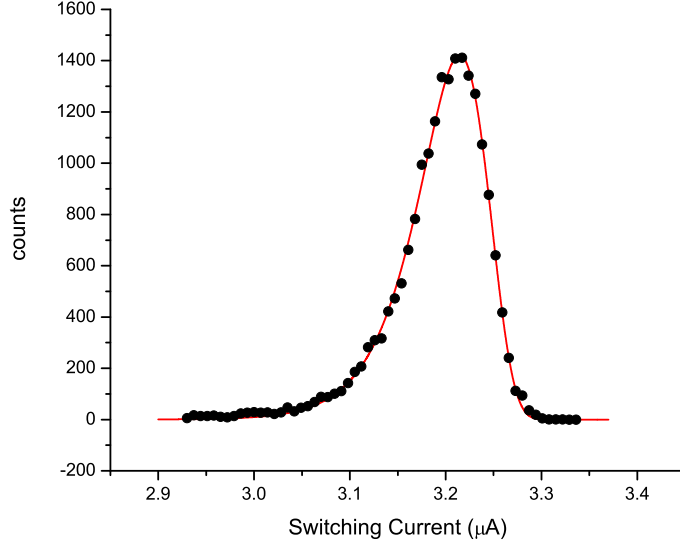
Figure 3.7: A measured histogram, fitted with the analytical expression presented in 3.3. The fit is comparable to the one in Fig. 3.3

good results for fitting and analyzing high temperature data.

For the purpose of fitting a dc-SQUID magnetometer switching current histogram with the function mentioned above, the variable is bias current I rather than flux. It is convenient to rewrite the probability distribution in terms of the maxima and the widths of the fitting function. For this, we substitute u with a linear function, using the current I as a variable. I_{max} corresponds to the switching current at which the most switching events occur, which is of course generally lower than the critical current I_c.

$$Substitute: \ u = b \cdot I \ \ and \ \ X = e^{u_{max}}$$
$$where \ u_{max} = b \cdot I_{max}$$

$$P(u) = A \cdot X \cdot e^{-u - X \cdot e^{-u}}$$
$$P(I) = A \cdot e^{b \cdot I_{max}} e^{-b \cdot I - e^{b \cdot I_{max}} \cdot e^{-b \cdot I}}$$
$$P(I) = A \cdot e^{-b(I - I_{max}) - e^{-b(I - I_{max})}} \tag{3.13}$$

Rewriting the fitting function like this, A is an independent parameter

that determines the amplitude and b determines the width of the function. It rescales the argument of the probability distribution. c can be used as a prefactor not differing much from 1 that allows to shift the maximum I_{max} if necessary, making up for small errors in determining the maxima. Two ways of obtaining the maxima have been used: The data acquisition program allows to run a smoothing algorithm that can give a good estimate for the maxima, or the maxima can be obtained by independent preceding measurements of the distributions for each single fluxoid state. Including the parameter c as described, the probability distribution reads as

$$P(I) = A \cdot e^{-b(I-c\,I_{max})-e^{-b(I-c\,I_{max})}} \tag{3.14}$$

The independence of the parameters from each other is the biggest advantage of this approximation compared to the Kurkijärvi theory since it increases numerical stability. It allows one to provide the Levenberg-Marquardt-algorithm [33] for the fit with better initial guesses.

As described previously, we are confronted in our measurements with partially overlapping switching current distributions that correspond to different flux states of the qubit. The fitting function for this double distribution (with parameters B, d, f analogous to A, b, c) reads as

$$P(I) = A \cdot e^{-b(I-cI_{max,1})-e^{-b(I-cI_{max,1})}} + B \cdot e^{-d(I-fI_{max,2})-e^{-d(I-fI_{max,2})}} \tag{3.15}$$

Again in this formula, the factors c and f are included in front of the maximum currents $I_{max,i}$, $i = 1, 2$, respectively. For most measurements, c and f were fixed ($c, f = 1$) and the widths and maxima were previously obtained by independent measurements of the switching current distributions for the two states. This requires careful measurement of these parameters, using around five times more counts than for the distributions during the sweep.
After using the deconvolution method, the probability of the system being in a specific fluxoid state can be obtained by the ratio of the amplitudes $A/(A + B)$(in the case of equal widths). Once this assumption no longer holds, the ratio r is given by

$$r = \frac{A \cdot b}{B \cdot d + A \cdot b} \tag{3.16}$$

c and f cannot influence the ratio since they only shift the distribution function along the current axis.

For a more careful analysis of the data, it is possible to allow widths (b and
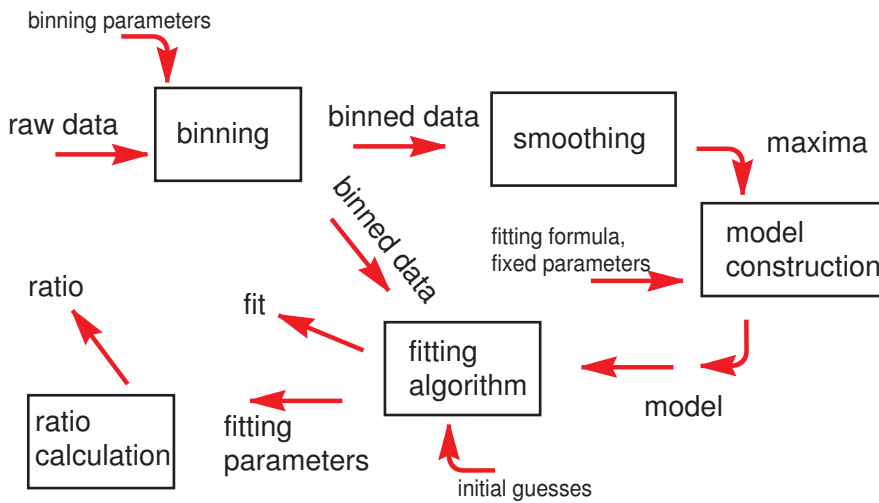
Figure 3.8: A scheme of the LabVIEW program, used to deconvolute switching current histograms in order to measure escape rates.

d) and maxima (*c* and *e*) to change by a small number in order to make up for statistical fluctuations. Unfortunately, this is restricted to the part of the transition where the ratios of left and right well are about equal ($0.2 < r < 0.8$), since the width as a free parameter is very sensitive to noise for statistics with a small number of counts.

3.4 A LabVIEW program using the analytical linear approximation

The theory presented before is used in a LabVIEW program to have direct data processing while measuring the current sample. The program consists of two parts, the first acquiring the data by interacting with the measurement electronics (2.2.1), the second one processing obtained raw data to give the probability of the system to be in one fluxoid state our the other for a given ϕ_x value. ϕ_x is swept along the edge of a hysteresis loop as shown in the flux-over-applied-flux graph Fig. 2.5. The code for second part is shown schematically in Fig. 3.8. Starting out from the raw switching distribution (like shown in Fig. 3.1), the raw data is first binned according to the histogram parameters provided by the user. These parameters include minimum and maximum switching current for the histogram and the number of bins.
The maxima of this histogram are then obtained by running a smoothing al-

gorithm using small adjacent averaging until the discrete approximation for the first derivative has only three (in the case of two peaks) or one (in the case of one peak) changes in sign. With the approximation for the first derivative, the coordinate of the maximum is calculated. Especially if the maxima are allowed to wiggle a bit (by $c, f \approx 1$), this provides sufficient accuracy. The method can fail if background noise masks one of the maxima or if resonances or noise strongly strengthen or weaken the appearance of switching events at certain current values, thus resulting in a spike (positive or negative) in the histogram.

The maxima are fed into the model constructing sub-VI, that mostly concatenates strings. It uses the formula from Eq. 3.15. A surrounding case structure selects the parameters required for the specific situation (sometimes it is more efficient to obtain values for some fitting parameters by preceding independent measurements).

The Levenberg-Marquardt algorithm then finds the best least-square-fit for the given parameters and the data. It converges quadratic locally, and as long as the initial guesses are good and the data is non-pathological, this procedure seems not to exhibit problems. Good initial guesses are relatively easy to provide, since at a fixed temperature the approximate width of the distribution is usually known, and it is good enough to start with guessing a third of the counts number for the amplitude. The time necessary to calculate the fitting parameters is negligibly small compared to the timescale of the data acquisition.

Fig. 3.9 visualizes the procedure. The data is binned within the given current limits (here 0.54 and 0.68 μA), and then a fit is obtained. Its parameters are used to calculate the probability of the system to be in one of the two fluxoid states, using Eq. 3.16.

Unfortunately, the given Levenberg-Marquardt fitting program does not allow one to limit the parameter range. Thus, control loops have to be implemented to validate the calculated fitting parameters and the resulting probability. The two major errors occurring in this experiment have been negative amplitude factors and extremely large widths, usually appearing in the case where one distribution is almost on the level of the background noise. Then, to make up for the noise (usually less than 5 counts/bin), the fitting algorithm can choose the width of one distribution to be very large, then basically fitting the background noise level. It also can happen that the amplitude is chosen to be a small negative value, making up for a little fluctuation at the position where the smaller distribution is expected to be. Both of these errors lead to wrong ratios, even greater than 1 in the latter case. A complete control loop has not been programmed since it seemed not necessary: We mostly worked with a
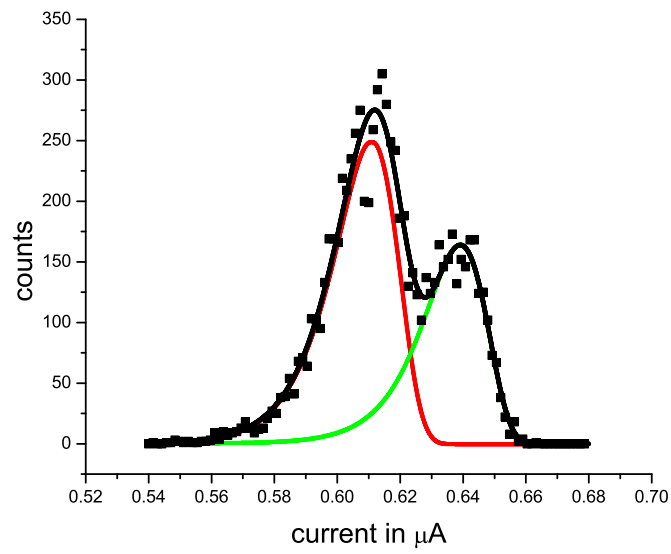
Figure 3.9: The black squares show a typical histogram as obtained from a switching distribution measurement. The black line is the fit given by the data acquisition program, the green line shows the single fit for the right and the red one for the left fluxoid state. The data has been acquired at 530 mK.

reduced number of parameters, having the width fixed and not allowing for maximum wiggling. Then, in the case of appearing negative amplitudes, they were automatically set to 0, which makes the ratio 0 or 1. These points are then unusable for the escape rate calculation, but appear in a region where escape rate calculation usually does not make sense anyway due to a very big signal-to-noise-ratio.

An almost object-oriented LabVIEW program has been written to reanalyze data in case of any unforeseen errors. It allows for manual changes in the parameters and the choice of the fitting function (comparing to Gaussian fit). It also provides a convolution tool to smoothen the data (a feature that is usually not used for analysis). With this program, all errors can be manually compensated.

Chapter 4

Analysis and conclusion

4.1 Introduction

After presenting the theory of the qubit and the measurement, this chapter intends to show some data obtained using the deconvolution method (Sec. 3.4). Furthermore, it will give some comparison first between the measured samples and then between the deconvolution method and the prior used threshold level method. The remainder of this chapter will then conclude this work and gives some outlook for future work.

4.2 Escape rate measurement data analysis

As explained in the preceding chapter, switching current distributions are measured at various values of applied qubit flux bias ϕ_x. Single switching events are measured 2000-4000 times, depending on the requirements of the statistics. The data is then deconvoluted using the program explained in Sec. 3.4. The amplitudes and the widths of the distributions for each states allow one to calculate the probability for the qubit state to be in one of the two wells (Eq. 3.16).

4.2.1 Probabilities

As the data acquisition program sweeps ϕ_x along the transition (the edge of the qubit hysteresis loop), the probability for the qubit of being in one of the two fluxoid states is obtained for each ϕ_x value. A typical measurement is shown in Fig. 4.1, using sample A. Since the qubit is initialized in the right well, the probability for being in the left well is initially zero. As we step the ϕ_x level, the potential is tilted further so that there is a nonzero probability of
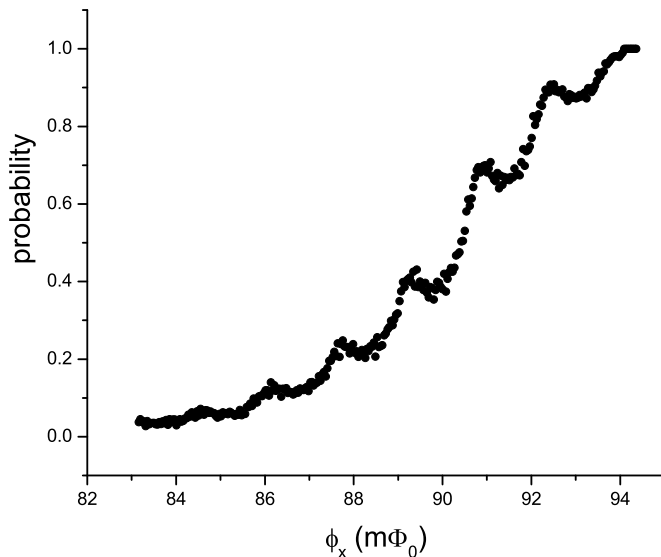
Figure 4.1: Sample A: The probability for the qubit to be in one of its states as a function of ϕ_x at 600 mK. The escape rates obtained from the same measurement are shown in Fig. 4.2

tunneling to the left well. The measurement shows peaks that are caused by an enhanced tunneling probability for well-aligned levels when levels in the left well are in resonance with levels in the right well. These data can be converted into escape rates as shown in the next subsection.

In a typical sweep, about 40 points have been measured between two peaks in order to get a sufficient resolution. In order to test the reproducibility of the data, every measurement has been repeated twice, introducing an offset in the ϕ_x values but keeping the step size the same. Furthermore, temperature stability has been monitored throughout the whole measurement process.

4.2.2 Conversion from probability to escape rates

The measured probability $P(\phi_x)$ can than be converted into escape rates $\Gamma(\phi_x)$ by

$$\Gamma(\phi_x) = \frac{1}{t_m} * ln\left(\frac{1}{1 - P(\phi_x)}\right) \tag{4.1}$$

where t_m is the amount of time that the potential is being tilted to allow for the qubit to escape into the other potential well. To determine the zero for the
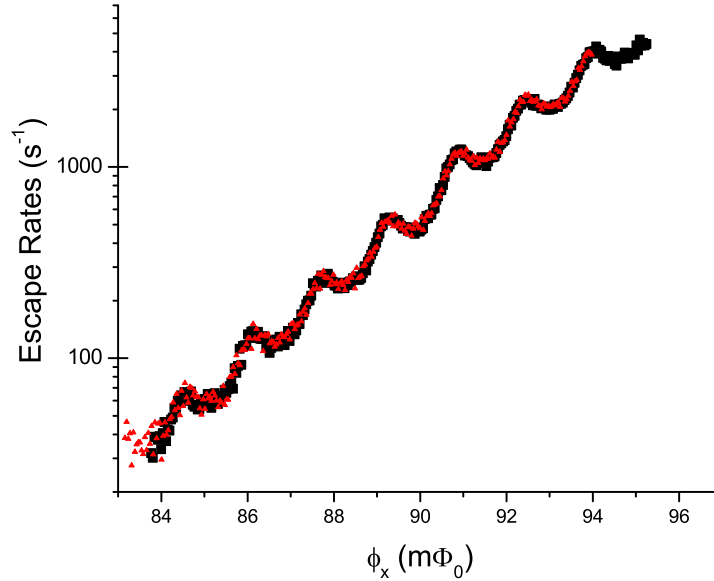
Figure 4.2: Sample A: The escape rates for the qubit for the escape from one fluxoid state to the other, measured on both sides of the loop (red triangles/black squares) at 600 mK. The escape rates are calculated using the measured probability as a function of qubit bias flux ϕ_x, shown in 4.1

applied flux bias ϕ_x, we have measured the escape rates on both edges of the $\phi - \phi_x$ hysteresis loop. When the zero for the ϕ_x bias is carefully calibrated, the escape rates for both sides coincide as can be seen in Fig. 4.2.

4.3 Temperature dependence of the thermal escape rates

To get a better understanding of the strength of the new data acquisition program, the same sample has been tested at 1.3 K, which is the base temperature of the cryostat if the ^{3}He is liquefied but not pumped. In this regime, the distributions are broader and their overlap becomes very strong. The escape rates calculated from this measurement are shown in Fig. 4.3. The peaks are broader than at lower temperatures but are still visible, as the levels given by the arrows indicate. The numerical ϕ_x values for the levels have been obtained using a program capable to calculate the levels based on the known qubit parameters. Formerly, due to the lack of a strong analysis tool, thermal escape
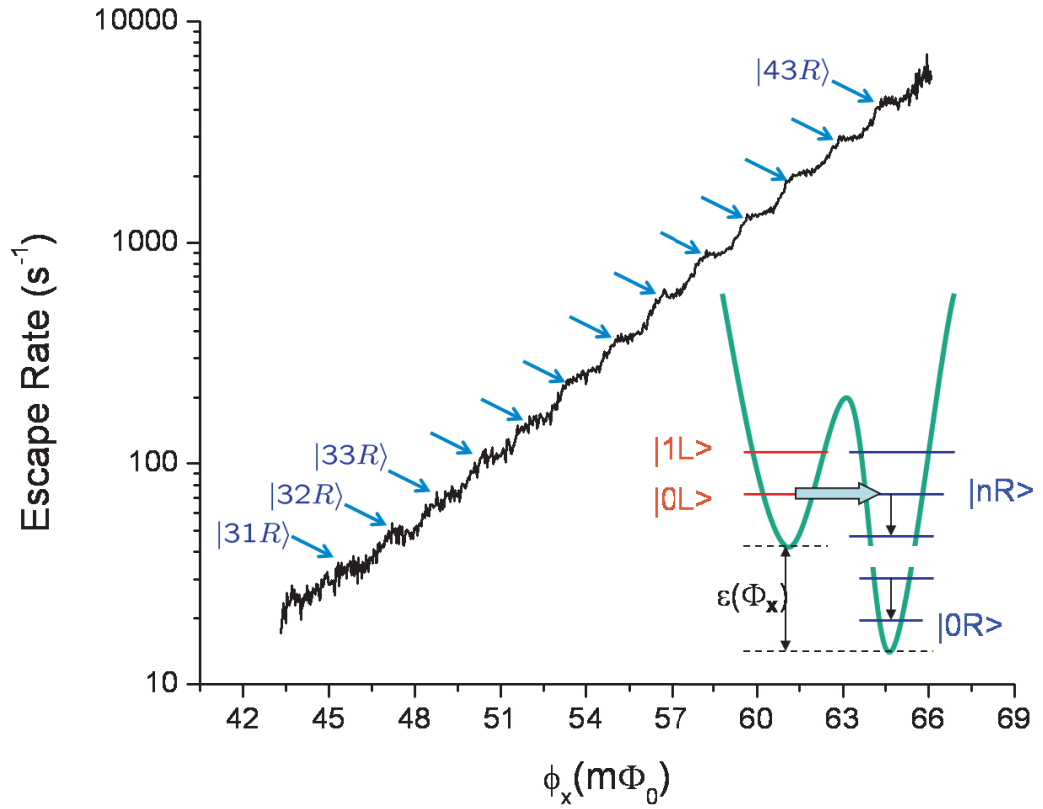
Figure 4.3: Sample A: Escape rates measured 1.3 K, using the deconvolution tool. The arrows mark the peaks corresponding to the given levels. The inset is a schematic of the potential, indicating the level terminology.
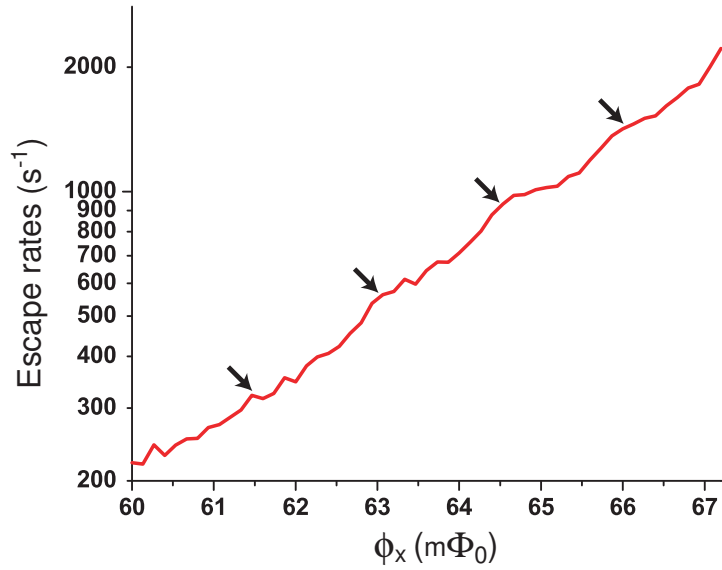
Figure 4.4: Sample B: Escape rates measured at 600 mK. Peaks have been calculated from the parameters and are marked with arrows.

rate data had only been obtained in a dilution refrigerator for temperatures between 10 and 600 mK [2]. The analysis of this data used a different method, called the threshold level method, that will be described and compared to the deconvolution method in section 4.5.

4.4   Comparison between samples

As already explained, the deconvolution method is meant to be used for sample comparison at temperature achievable with a ^{3}He-cryostat, allowing for a faster diagnostic since a ^{3}He-cryostat requires less preparation time and less liquid helium, than a dilution refrigerator. Therefore, after having proved the efficiency of the analysis method on a well known sample (Sample A), we have proceeded toward testing a newly fabricated sample (Sample B).
Unfortunately, sample B displayed a worse behavior than sample A, as shown in Fig. 4.4. Fig 4.5 shows that also for sample B the fluxoid states are well separated and the analysis of the switching distribution is within the capability of the deconvolution method. Thus, the results must be due to the process and material changes.
In recent years the problem of material optimization for better qubit performance has become more and more important after the discovery by Martinis'
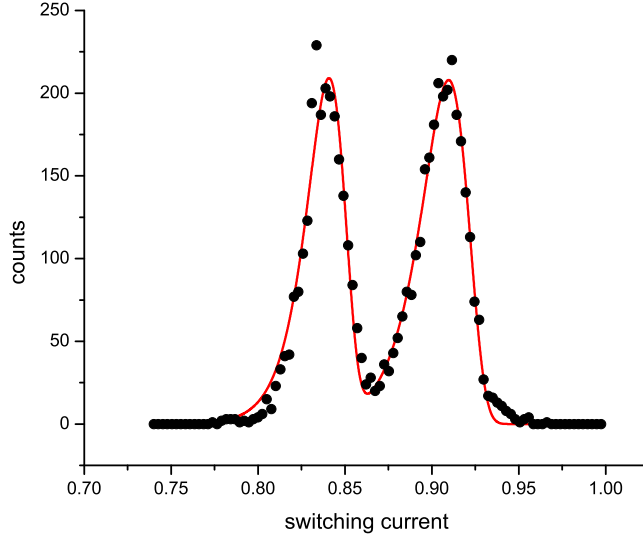
Figure 4.5: Sample B: Switching current histogram measured at 600 mK, fitted with the analytical expression derived in the last chapter. The agreement with this approximation is not as good as in Fig. 3.7, which is due to sample properties.

group [34, 35] of the presence of two level fluctuators (TLF) in the dielectrics that tend to couple to the qubit with results that are detrimental to coherence times.

In the effort to reduce the effect of TLF on our qubit work is in progress toward optimizing the fabrication process. Our process is based on $Nb/AlO_x/Nb$ trilayer technology and is described in references [36, 37].

The second sample showed in this thesis (sample B) differs from sample A in having most of the qubit pattern in a Nb wiring layer (counter-electrode), as opposite to having the qubit mostly patterned in the $Nb/AlO_x/Nb$ layer (base electrode). This reduced the amount of AlO_x dielectric in direct contact with the qubit. Another difference between the two samples was in the choice of the substrate. In general the resistivity of a silicon substrate should indicate the level of defects. Sample A was fabricated on a silicon wafer with a resistivity of 20 Ωcm , while for sample B a silicon wafer with 15 kΩcm was chosen.
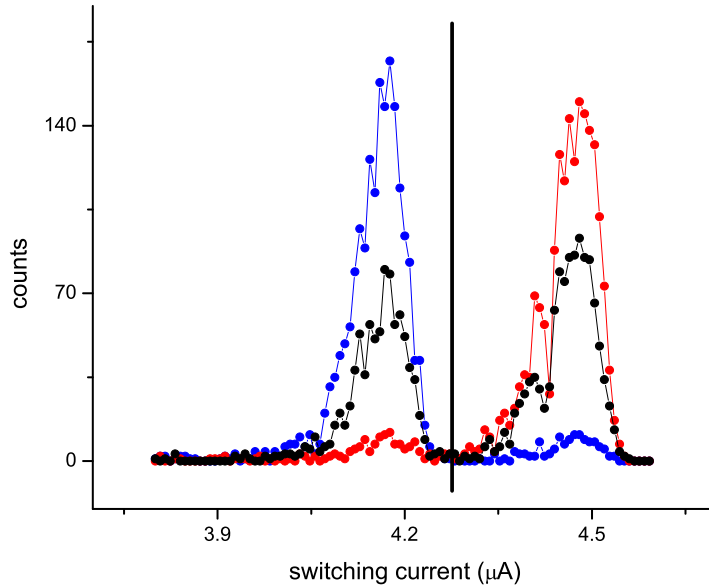
Figure 4.6: Sample A: The threshold in use to distinguish the two states, shown at three values for ϕ_x. Each histogram measurement had a total of 4,000 counts. The escape rates obtained from the same measurement are shown in Fig. 4.7

4.5 Comparison to a formerly used method in data analyzing

For an easier analysis, we used the so called threshold method to distinguish the two states. Fig. 4.6 shows how the threshold is set; the probability is then simply defined as the number of counts below the threshold divided by the total number of counts. This procedure is very effective as long as the distributions are nicely separated, as it is the case for sufficiently low temperatures. As our work is in the regime of higher temperatures, this is not always the case. For sample A at 600 mK problems happen to arise as the probability comes close to 0 or 1. This effect is caused by the long left tail of each distribution which might mask some counts of the other fluxoid state.
Fig. 4.7 shows how the threshold method starts to fail as the distributions get broader and overlap more. For the green plot on one side of the qubit hysteresis loop, the values for the highest rates do not agree with the other three, and the same is the case for the red on the other side of the loop in
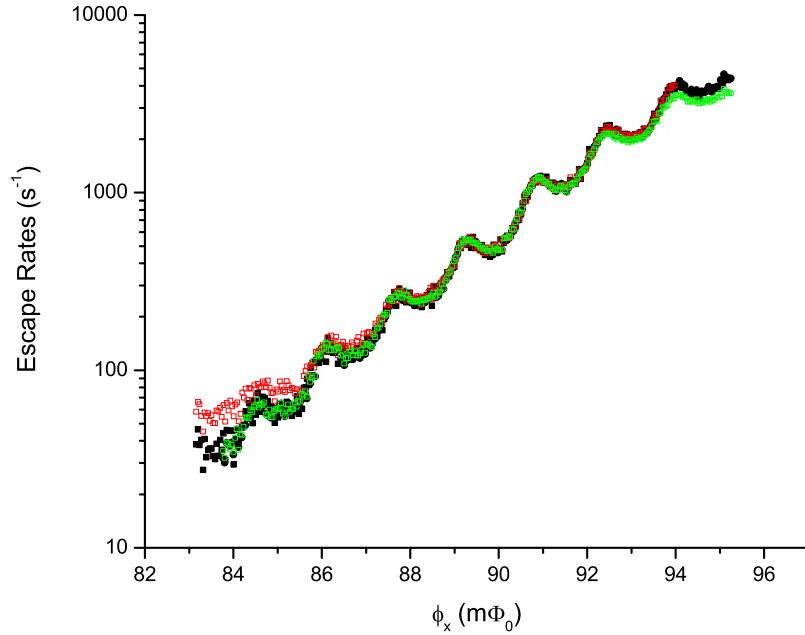
49

Figure 4.7: Escape rates, measured at 600 mK on both sides of the hysteresis loop, analyzed with the deconvolution method (black dots and squares) and the threshold method (red squares for the right edge of the hysteresis loop and green squares for the left edge), plotted versus ϕ_x.

case of the lowest rates. Especially the slope in these parts does not agree any longer, and the first/last peak is disguised.

These data clearly show the limits of the threshold method at temperature higher than 600mK when the width of the switching distribution is more and more broadened by thermal effects. As samples should be characterized in a [3]He-cryostat, fast diagnosis requires both the capability to measure at higher temperatures and also to measure distributions that overlap more than the one shown. Especially in the latter case the long tail of the distribution makes a threshold-based analysis impossible.

4.6 Conclusion

In this thesis, a deconvolution method for fast sample diagnosis has been developed. It uses the peak-to-valley ratio in the thermal escape rate measurement as an indicator to decide upon the quality of a sample. Although

the theory has been originally developed for an rf-SQUID, it was found to be suitable for the dc-SQUID magnetometer as well. The deconvolution method allows to observe quantum mechanical behavior with surprisingly good results for data up to 1.3 K, which is an improvement as former measurements only went up to 600 mK. Before, only classical properties of the qubit samples have been tested at these temperatures, leaving the test of the quantum mechanical properties to measurements in a dilution refrigerator. The capability of obtaining data in sufficient quality at higher temperatures gives a fast feedback for the sample fabrication. Now, the quality of new samples can be determined using a ^{3}He-cryostat which is less liquid Helium consuming and requires less time for the cool down and the warm up process.

For the measured sample B it can be clearly concluded that it has not been an improvement. Although the changes explained in Sec. 4.4 were expected to improve sample quality and decoherence times, this was not the case. One possible cause for this might be that the qubit is stronger influenced by the insulating dielectric SiO_2 where two level fluctuators are present. This property is highly sensitive to the fabrication process. Furthermore, the switch to high resistivity silicon wafers seems not to improve sample quality (see comparative measurements shown in [2]), thus future samples might focus on using low-resistivity substrates.

Bibliography

[1] Valérie Lefevre-Seguin, Emmanuel Turlot, Cristian Urbina, Daniel Esteve, and Michel H. Devoret. Thermal activation of a hysteretic dc superconducting quantum interference device from its different zero-voltage states. *Phys. Rev. B*, 46(9):5507–5522, Sep 1992. doi: 10.1103/PhysRevB. 46.5507.

[2] Douglas A. Bennett. *Studies of decoherence in rf SQUID Qubits*. PhD dissertation, Stony Brook University, Department of Physics and Astronomy, December 2007.

[3] John M. Martinis, Michel H. Devoret, and John Clarke. Experimental tests for the quantum behavior of a macroscopic degree of freedom: The phase difference across a Josephson junction. *Phys. Rev. B*, 35(10):4682–4698, Apr 1987. doi: 10.1103/PhysRevB.35.4682.

[4] Heike Kamerlingh Onnes. The superconductivity of mercury. *Leiden Comm.*, 122,124, 1911.

[5] Walther Meissner and Robert Ochsenfeld. Ein neuer Effekt bei Eintritt der Supraleitfähigkeit. *Die Naturwissenschaften*, 21:787, 1933.

[6] Heinz London and Fritz London. *Proc. Roy. Soc.*, A 149:71, 1935.

[7] John Bardeen, Leon N. Cooper, and John R. Schrieffer. Theory of superconductivity. *Phys. Rev.*, 108(5):1175–1204, 1957.

[8] Website of the nobel committee, 2008. URL http://nobelprize.org/nobel_prizes/physics/laureates/.

[9] Michael Tinkham. *Introduction to Superconductivity*. Dover Publications, 2004.

[10] Brian D. Josephson. Possible new effects in superconductive tunnelling. *Physics Letters*, 1(7):251–253, 1962. doi: 10.1016/0031-9163(62)91369-0.

[11] S. Levy, E. Lahoud, I. Shomroni, and J. Steinhauer. The a.c. and d.c. Josephson effects in a Bose Einstein condensate. *Nature*, 449:579–583, 2007. doi: 10.1038/nature06186.

[12] Shannon Kdoah Range (NASA). Gravity probe b: Investigating Einsteins spacetime with gyroscopes, October 2004. URL http://einstein.stanford.edu/content/education/GP-B_T-Guide4-2008.pdf.

[13] Konstantin Likharev. *Dynamics of Josephson Junctions and Circuits*. Gordon Breach Science Publishers, 1986.

[14] Siyuan Han, J. Lapointe, and J. E. Lukens. Effect of a two-dimensional potential on the rate of thermally induced escape over the potential barrier. *Phys. Rev. B*, 46(10):6338–6345, Sep 1992. doi: 10.1103/PhysRevB.46.6338.

[15] S. Han, J. Lapointe, and J. E. Lukens. Thermal activation in a two-dimensional potential. *Phys. Rev. Lett.*, 63(16):1712–1715, Oct 1989. doi: 10.1103/PhysRevLett.63.1712.

[16] R. Rouse, Siyuan Han, and J. E. Lukens. Observation of resonant tunneling between macroscopically distinct quantum levels. *Phys. Rev. Lett.*, 75(8):1614–1617, Aug 1995. doi: 10.1103/PhysRevLett.75.1614.

[17] Richard P. Rouse. *Macroscopic Quantum Phenomenia in an rf SQUID*. PhD dissertation, Stony Brook University, Department of Physics and Astronomy, August 1996.

[18] David P. DiVincenzo. The physical implementation of quantum computation. *Fortschritte der Physik*, 48:9, 2000.

[19] V Patel and JE Lukens. Self-shunted $Nb/AlO_x/Nb$ Josephson junctions. *IEEE Transactions Applied Superconductivity*, 9:3247–3250, 1999.

[20] D. Nakada, K.K. Berggren, E. Macedo, V. Liberman, and T.P. Orlando. Improved critical-current-density uniformity by using anodization. *IEEE Transactions on Applied Superconductivity*, 13:111, 2003.

[21] M.M. Khapaev, A.Yu. Kidiyarova-Shevchenko, P. Magnelind, and M.Yu. Kupriyanov. 3D-MLSI: software package for inductance calculation in multilayer superconducting integrated circuits. In *IEEE Transactions on Apllied Superconductivity*, pages 1090–1093, 2001.

[22] S. Pottorf. *Subgap quasiparticle transport and low frequency critical current fluctuations in Nb/AlO$_x$/Nb Josephson junctions*. PhD dissertation, Stony Brook University, Department of Physics and Astronomy, December 2007.

[23] Guy K. White. *Experimental techniques in low-temperature physics*. Oxford Science Publications, 1989.

[24] Theodore Van Duzer and Charles W. Turner. *Principles of Superconductive Devices and Circuits*. Prentice Hall, 1999.

[25] H. A. Kramers. Brownian motion in a field of force and the diffusion model of chemical reactions. *Physica*, 7:284, 1940.

[26] Juhani Kurkijärvi. Intrinsic fluctuations in a superconducting ring closed with a Josephson junction. *Phys. Rev. B*, 6(3):832–835, Aug 1972. doi: 10.1103/PhysRevB.6.832.

[27] M. Büttiker, E.P. Harris, and R. Landauer. Thermal activation in extremely underdamped Josephson-junction circuits. *Phys. Rev. B*, 28: 1286–1275, 1983.

[28] T.A. Fulton and L.N. Dunkleberger. Lifetime of the zero-voltage state in Josephson tunnel junctions. *Phys. Rev. B*, 9:4760–4768, 1974.

[29] Patrick A. Lee. Effect of noise on the current-voltage characteristics of a Josephson junction. *Jour. App. Phys.*, 42:325–334, 1971.

[30] Shao-Xiong Li, Yang Yu, Yu Zhang, Wei Qiu, and Siyuan Han. Quantitative study of macroscopic quantum tunneling in a dc SQUID: A system with two degrees of freedom. *Phys. Rev. Lett.*, 89(9):98301, 2002.

[31] Daniel B. Schwartz. *Tunneling of a heavily damped macroscopic variable*. PhD dissertation, Stony Brook University, Department of Physics and Astronomy, December 1986.

[32] D. B. Schwartz, B. Sen, C. N. Archie, and J. E. Lukens. Quantitative study of the effect of the environment on macroscopic quantum tunneling. *Phys. Rev. Lett.*, 55(15):1547–1550, Oct 1985. doi: 10.1103/PhysRevLett. 55.1547.

[33] Donald Marquardt. An algorithm for least-squares estimation of nonlinear parameters. *SIAM Journal on Applied Mathematics*, 11:431–441, 1963. doi: 10.1137/0111030.

[34] R. W. Simmonds, K. M. Lang, D. A. Hite, S. Nam, D. P. Pappas, and John M. Martinis. Decoherence in Josephson phase qubits from junction resonators. *Physical Review Letters*, 93(7):077003, 2004. doi: 10. 1103/PhysRevLett.93.077003. URL http://link.aps.org/abstract/PRL/v93/e077003.

[35] John M. Martinis, K. B. Cooper, R. McDermott, Matthias Steffen, Markus Ansmann, K. D. Osborn, K. Cicak, Seongshik Oh, D. P. Pappas, R. W. Simmonds, and Clare C. Yu. Decoherence in Josephson qubits from dielectric loss. *Physical Review Letters*, 95(21):210503, 2005. doi: 10.1103/PhysRevLett.95.210503. URL http://link.aps.org/abstract/PRL/v95/e210503.

[36] Wei Chen, Vijay Patel, and James E. Lukens. Fabrication of high-quality Josephson junctions for quantum computation using a self-aligned process. *Microelectronic Engineering*, 73-74:767, 2004.

[37] Vijay Patel, Wei Chen, Shawn Pottorf, and James E. Lukens. A fast turn-around time process for fabrication of qubit circuits. *IEEE Transactions on Apllied Superconductivity*, 15:117, 2005.